Study of the Impact of Ice Formation in Leads upon the Sea Ice Pack Mass Balance Using a New Frazil and Grease Ice Parameterization

Alexander V. Wilchinsky, Harold D. B. S. Heorton, and Daniel L. Feltham

Centre for Polar Observation and Modelling, Department of Meteorology, University of Reading, Reading, United Kingdom

Paul R. Holland

British Antarctic Survey, Cambridge, United Kingdom

ABSTRACT

Leads are cracks in sea ice that often form because of deformation. During winter months, leads expose the ocean to the cold atmosphere, resulting in supercooling and the formation of frazil ice crystals within the mixed layer. Here the authors investigate the role of frazil ice formation in leads on the mass balance of the sea ice pack through the incorporation of a new module into the Los Alamos sea ice model (CICE). The frazil ice module considers an initial cooling of leads followed by a steady-state formation of uniformly distributed single size frazil ice crystals that precipitate to the ocean surface as grease ice. The grease ice is pushed against one of the lead edges by wind and water drag that the authors represent through a variable collection thickness for new sea ice. Simulations of the sea ice cover in the Arctic and Antarctic are performed and compared to a model that treats leads the same as the open ocean. The processes of ice formation in the new module slow down the refreezing of leads, resulting in a longer period of frazil ice production. The fraction of frazil-derived sea ice increases from 10% to 50%, corresponding better to observations. The new module has higher ice formation rates in areas of high ice concentration and thus has a greater impact within multiyear ice than it does in the marginal seas. The thickness of sea ice in the central Arctic increases by over 0.5 m, whereas within the Antarctic it remains unchanged.

1. Introduction

In turbulent, impure supercooled waters, ice forms as small thin circular crystals around 1 mm in diameter with a width of up to 100 times smaller (Martin and Kauffman 1981; Daly 1994). Despite their small size, the crystals can quickly aggregate and form significant volumes of ice in rivers, lakes, and oceans. Information about the relative fractions of frazil and congelation ice can be taken from sea ice cores. This comparison assumes that granular ice within the ice core is frazil in origin and columnar ice is congelation in origin. The cores are point observations often taken from the center of stable floes so the values discussed here are only an indication of the relative fractions of ice, but represent the best available data. Observations in the Antarctic show that a high fraction of frazil ice is present in the sea ice cover. In particular in the Weddell Sea, Gow et al. (1982) estimated the frazil ice fraction to be as much as 50%, occasionally reaching 90%. Clarke and Ackley (1984) found on average a 70% fraction of frazil ice off of Maud Rise. In coastal waters of the eastern and southern Weddell Sea, Lange (1988) reported the typical floe structure was 5%–10% of snow ice, 50%–60% of frazil ice, 20%–30% of congelation ice, and 20%–30% of platelet ice. Studying development of sea ice in coastal waters of the southern Weddell Sea, Eicken and Lange (1989) observed that the sea ice structure depended on conditions during its formation: as the wind speed was increasing from below $3 \, \text{m s}^{-1}$ to more than $10 \, \text{m s}^{-1}$, the sea ice structure was changing from mainly columnar ice (ice forming onto existing sea ice) through intermediate columnar/granular to mainly granular ice (a mixture of congealed frazil and grease ice), formed through aggregation of frazil ice. At high wind speeds

frazil ice was swept underneath the sea ice. In the western Ross Sea, Jeffries and Weeks (1992) observed a frazil ice fraction varying from 2.3% to 88.5% with a mean of 38.5% ± 27%. Similarly, high frazil ice concentrations were found in the Indian Ocean sector (Allison and Qian 1985; Jacka et al. 1987; Tison and Haren 1989).

In contrast, the Arctic ice has a smaller fraction of frazil ice; for example, Eicken et al. (1995) found 61% of undeformed columnar, 9% of deformed ice, and 18% of frazil ice in the central Arctic multiyear ice. Such a striking difference in the Arctic and Antarctic sea ice structure is explained through the presence of a much higher fraction of first year ice formed around Antarctica where the sea ice area decreases by around 80% over summer. Observing the sea ice development across the Antarctic sea ice rim in the Weddell Sea, Lange et al. (1989) found that the frazil ice was dominant in the northern part of the sea ice rim close to the advancing sea ice edge, as it was the primary material for formation and consolidation of pancake floes. Farther away, inshore from the advancing edge, the smaller size of open water areas, mainly consisting of leads, resulted in the decreasing of wind catchment area, attenuation of surface waves, and weaker frazil ice production. Consequently, congelation ice was found mainly in thin floes representing refrozen leads under calm conditions.

Given the importance of frazil ice in the formation of Antarctic sea ice, its realistic description in sea ice models is crucial for determination of the Antarctic sea ice structure. Different sea ice structures have different brine layer spacings depending on the grain size (Nakawo and Sinha 1984; Lange 1988) and affect salt drainage into the ocean, as well as the salinity of the sea ice. A standard parameterization of frazil ice formation is to calculate the volume of frazil ice required to remove, through latent heat release, supercooling of the ocean water (e.g., Kantha 1995; Hunke and Lipscomb 2010; Vancoppenolle et al. 2009). Supercooling occurs as heat is lost through the water–air interface either in the marginal ice zone or within leads formed through sea ice deformation. The Los Alamos sea ice model (CICE; Hunke and Lipscomb 2010) then produces new ice by putting all the volume of frazil ice calculated in this way into a constant thickness layer (5 cm in the standard configuration) until no more open water is left and then adding the remaining volume to the sea ice bottom. The Louvain-la-Neuve sea ice model (LIM3; Vancoppenolle et al. 2009) as part of a coupled ice–ocean hindcast model (LIM-NEMO) uses a more sophisticated algorithm with a variable collection thickness (5–15 cm) from a polynya model by Biggs et al. (2000). The collection thickness depends on the wind and sea ice speed

and is calculated using the balance between the inertial and gravity forces in the wedge of an advancing grease ice layer (Bauer and Martin 1983). This model, however, does not consider how the grease ice layer takes shape under the wind and ocean drag. LIM3 produces 38% of Antarctic sea ice through frazil ice collection (Vancoppenolle et al. 2009).

Frazil ice crystals are initially seeded by a contaminant within the water (e.g., a speck of dust or a fragment of another crystal) and then distributed throughout the mixed layer through turbulent mixing (Daly 1994). The crystals then grow and collide and fracture to seed more crystals. It is also possible for crystals to aggregate into larger masses, though this is often assumed unlikely when the water is turbulent except at the surface where crystals aggregate to form grease or pancake ice. As the crystals size increases, so does their buoyancy, making the crystals rise faster. Turbulent mixing results in large- and medium-sized crystal numbers decreasing by an order of magnitude within 10 m from the surface, while the number of small-sized crystals increases over the same depth, as was shown by Svensson and Omstedt (1998) using a κ–ϵ turbulent mixing model. Sophisticated frazil ice dynamics models such as this, as well as those by Omstedt and Svensson (1984), Omstedt (1985), and Holland and Feltham (2005), normally assume horizontal uniformity. Although the lead width can be much larger than the mixed layer thickness over which the frazil ice dynamics is modeled, the 1D models are still limited as they do not account for transportation of the mixed layer water into the lead (Kozo 1983; Morison et al. 1992; Kantha 1995). Rising frazil crystals collect at the surface of the lead as a layer of grease ice, a mixture of frazil crystals and seawater that is herded toward one side of the lead by the wind and ocean currents. The way in which grease ice is herded affects the open water fraction in the lead and thus the heat flux from the lead and the amount of new frazil ice produced. The extent and profile of herded grease ice has been modeled by Smedsrud (2011) using a balance between air and water drag and granular resistance.

As frazil ice is transported underneath sea ice it gets deposited on the sea ice bottom (McGuinness et al. 2009). This problem was addressed by Skyllingstad and Denbo (2001), who considered a coupled frazil ice–ocean model using a large eddy simulation. Despite the big advantage of this model over the previous ones, incorporating a coupled ocean–frazil ice model into a climate model would be problematic because of its complexity. Moreover, as Wang and Doering (2005) showed, matching the model with different experimental data required assuming different initial conditions and model parameters, which poses a problem of
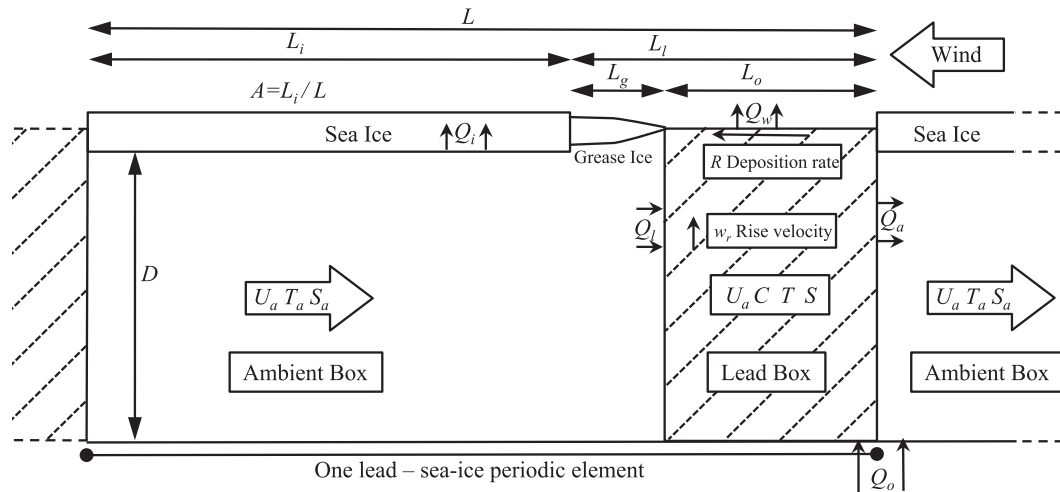
FIG. 1. A vertical cross section of the idealized lead–sea ice structure.

choosing such parameters. There are other additional processes that play a role in ice formation that are also not currently considered by sea ice climate models (Hunke et al. 2011; Maslowski et al. 2012), for example, pancake ice formation (Hopkins and Shen 2001) and tides (Holloway and Proshutinsky 2007).

The aim of this paper is to investigate the role of lead-specific dynamics of frazil and grease ice formation upon the whole sea ice pack. This is achieved through the development of an improved parameterization of ice formation in leads that accounts for the following processes in a simple but physically consistent manner:

1) the dynamics of frazil ice formation in supercooled waters under a lead describing the rate of its production, surface collection, and grease ice formation (section 2);
2) the transportation of the mixed layer and frazil crystals between the ice-covered and ice-free parts (section 3); and
3) the shape of the grease ice layer under the wind and water drag following Smedsrud (2011) (appendix A).

This parameterization has been incorporated into the CICE model (section 4a and appendix B), which does not currently consider the processes listed above. The model is run in both the Antarctic (section 4b) and Arctic (section 4c) and is compared to the old sea ice formation scheme. The sensitivity to parameters is considered in both the old and new models to show the effect our more sophisticated scheme has on the dynamics of sea ice formation and the state of sea ice pack as a whole. We show how the consideration of lead specific processes of frazil ice formation can increase the frazil ice fraction by a factor of 5 to 40% of the overall

formation rate (Figs. 4d, 6d). This redistribution of ice formation changes the spatial distribution of sea ice and increases the thickness of multiyear sea ice (Fig. 7h).

2. Frazil ice formation in a single lead

a. Idealized representation of the lead–sea ice structure

In our formulation, a bulk model with no spatial variation represents the ocean beneath the lead. The lead is assumed to be much longer than its width, with the lead characteristics defined by its cross-sectional length scales shown in Fig. 1, with key mathematical notation listed in Table 1. To make our model tractable, similar to Kantha (1995), we consider a lead by splitting the mixed layer under the sea ice into a box under the lead (the lead box) and a box under the sea ice (the ambient box). We assume that all properties are spatially uniform over each box and develop in time with a step change at their boundaries, implying instantaneous vertical and horizontal mixing within the box. As the main difference between the two boxes is the amount of heat loss to the atmosphere, we assume that the area covered by grease ice belongs to the ambient box as the heat loss over the grease ice is assumed to freeze water within grease ice, while the heat lost over the rest of the lead cools down the lead box. The lead and ambient boxes have different properties that are exchanged through fluxes at the boxes' interface. Frazil ice formation occurs only in the lead box, with frazil ice concentration taken as an average over the depth, and only one representative crystal size is considered similar to Jenkins and Bombosch (1995). While frazil ice is formed only in the

TABLE 1. Key mathematical notations.

Notation	Description
A	Areal sea ice concentration
C	Frazil ice concentration
L	Length
Q	Heat flux
R	Frazil ice deposition
S	Salinity
t	Temperature
U	Water speed
V	Grease ice volume
$V^{f,g,w}$	Frazil, grease, water volume flux
t	Time
w'	Volume of water turning into ice
ρ	Density
ξ	Frazil formation probability
τ_c	Applied stress on grease ice
K_r	Grease ice strength
Constants	
D	Mixed layer depth
H_f	Latent heat of fusion
L	Sea ice and lead structure length
c_w	Specific heat of water
r	Frazil crystal radius
η	Grease ice fraction
κ	Heat transfer coefficient
ϕ	Grease ice internal friction angle
θ_l	Angle between lead and drag
Subscripts	
a, m	Ambient box, mixed layer
f	Freezing
i, g, c	Sea ice, grease ice, both combined
j	CICE sea ice thickness category
l, o	Lead, ocean
s	Steady state
w	Water
max, min	Maximum, minimum

be linked to the layer salinity under sea ice (Petty et al. 2014) and horizontal mixing rates vary over the depth of the water beneath the lead during frazil ice formation (Skyllingstad and Denbo 2001). However, errors made because of the lack of vertical variation in our model will be less than the errors made by the existing treatment of frazil formation in leads as they also assume that there is no variation between the lead and the ambient part of the mixed layer. We have chosen these simplifications in order to focus upon the relationship between horizontal extent of leads and frazil formation rates over the whole sea ice pack. The consideration of the variations in the vertical structure of the ocean beneath leads over the sea ice pack is a possible topic of substantial future study.

Considering an arbitrary area of continuous sea ice cover, or sea ice model grid cell, which contains solid sea ice floes and leads, the gaps between them, the following model equations are derived. Given the sea ice concentration A, we assume that in a particular sea ice model grid cell, leads of the same width L_l are aligned and positioned uniformly, separated by $L_i = AL_l/(1 - A)$ wide spans of sea ice in the transverse direction, as depicted in Fig. 1. Here $A = L_i/L$ is the sea ice areal fraction and $(1 - A)$ is the fractional area of the lead including grease ice. The width of the lead–sea ice structure $L = L_i + L_l$ is assumed to be constant. However, the lead width L_l changes because of deformation and lateral melting/freezing, which results in changes of sea ice concentration A. Similarly, the open water width L_o and the grease ice width $L_g = L_l + L_o$ depend on the volume of grease ice and the wind and water drag on the grease ice. We will also use areal fractions of open water $A_o = L_o/L$, grease ice $A_g = L_g/L$, and area covered by sea and grease ice $A_c = A_g + A$.

Associating our coordinate system with the lead, the sea ice motion is represented as the transportation of the mixed layer across the lead. We assume the mixed layer has depth $D = 20$ m and that there is little mixing with the underlying water. The only modeled interaction between the mixed layer and deep ocean is the heat flux Q_o, prescribed in this study by the CICE model forcing. The water characteristics in the lead box under the lead are given by its temperature T, salinity S, and frazil ice concentration C, the volume of frazil ice per unit volume of the lead box. The seawater in the ambient box is represented by T_a and S_a, and both boxes have the same ambient water speed perpendicular to the lead U_a. While water is transported between both boxes and frazil ice is transported into the ambient box, we do not consider frazil ice concentration evolution in the ambient box; rather, the volume of the frazil ice transported into the ambient box is accounted for through an equivalent supercooling that would generate the same

lead box, it is transported to the ambient box through the box interface with the fluid movement between the boxes assumed to dominate diffusion, which is neglected. Since Skyllingstad and Denbo (2001) tuned their single crystal size model in order to fit the Lead Experiment (LEADEX) data of lead observations (Levine et al. 1993), we chose the same parameters for our model, in particular the crystal radius r in Eq. (2) below.

The lack of vertical variation, a constant mixed layer thickness, and a single frazil crystal size are significant simplifications from previous process models of frazil ice formation. These simplifications are made despite observations of the variable vertical structure of the ocean beneath cracks in the sea ice (Dmitrenko et al. 2010) and the varying freezing temperature of water with depth and pressure (McDougall et al. 2014). In particular variations in the depth of the mixed layer are known to

amount of ice at its freezing temperature. At each time step, this supercooling of the ambient box, along with any supercooling from the transportation of water from the lead box, is removed and the equivalent volume of frazil ice is immediately added to the bottom of the sea ice. The characteristics of the mixed layer as a whole T_m and S_m are found by weighting the lead and ambient box characteristics by their widths with $T_m = A_o T + A_c T_a$, $S_m = A_o S + A_c S_a$. The net downward heat flux is Q, which is the difference between the heat flux from air to the water Q_s (negative in winter) and the flux from the mixed layer to the deep ocean Q_o. Here we consider frazil ice consisting only of one size frazil crystals of a disk shape with radius $r = 1$ mm and aspect ratio $a_r = 0.01$.

b. Balance equations for the temperature, salinity, and frazil ice concentration in the lead box

Within the lead box, all characteristics are uniformly distributed and can be described by standard conservation equations (e.g., Jenkins and Bombosch 1995). The frazil ice concentration C changes because of heat loss to supercooled water at frazil ice crystal edges, heat gain from warmer water, buoyancy rising, and sea surface removal (conversion into grease ice), as well as transportation out of the box with the relation

$$\dot{C} = \left[\kappa(T_f - T) - R - \frac{U_a}{L_o} \right] C, \qquad (1)$$

where $\dot{C}$ is Newton's time derivative of C, T_f is the freezing temperature, T is the water temperature, R is the frazil ice surface deposition rate, U_a is the mixed layer speed, and L_o is the length of open water.

The first term on the rhs of Eq. (1) describing the heat loss is proportional to the difference between the frazil ice (freezing) temperature T_f and the water temperature T with the heat transfer coefficient κ given by

$$\kappa = \frac{2 \mathrm{Nu} k_w}{a_r r^2 H_f \rho_i}, \qquad (2)$$

where the Nusselt number Nu = 1, the thermal conductivity of the laminar layer of seawater surrounding the frazil crystal is $k_w = 0.564$ W m^{-1} °C^{-1}, the latent heat of fusion is $H_f = 3.34 \times 10^5$ J kg^{-1}, and the ice density is $\rho_i = 920$ kg m^{-3}. The ice freezing temperature depends on water salinity S and is taken to be $T_f = -\mu S$, where $\mu = 0.054$ psu °C^{-1} and the pressure dependence is ignored since we are concerned with frazil ice only in the ocean mixed layer.

The second term on the rhs of Eq. (1), R, describes the rising of the crystals followed by their merging with the
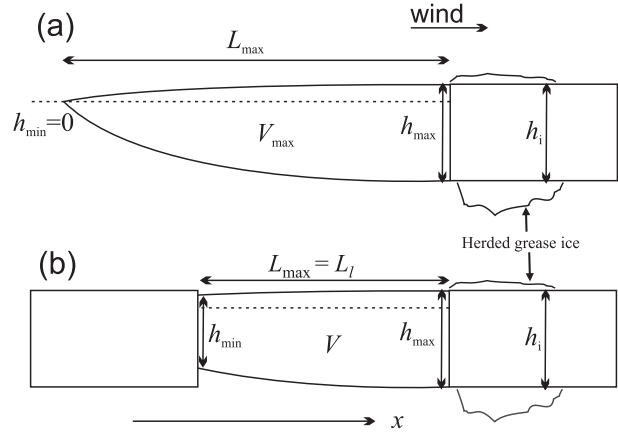

FIG. 2. Grease ice distribution in the lead (a) when the lead is wide enough to accommodate all grease ice and (b) when it is not.

grease ice. We assume that the lead is not wide enough to ensure significant reduction of vertical mixing caused by the shear from the underside of the sea ice, so we describe R, the frazil ice deposition on top, following Jenkins and Bombosch (1995) with

$$R = \frac{w_r}{D} \left(1 - \frac{U_a^2}{U_{\mathrm{cr}}^2} \right) \mathcal{H} \left(1 - \frac{U_a^2}{U_{\mathrm{cr}}^2} \right), \qquad (3)$$

where $w_r = 1.65 \times 10^{-3}$ m s^{-1} is the crystal buoyancy rising velocity for a crystal as described above, while the second factor models the opposition to rising of the crystals by turbulence, completely suppressing it when the mixed layer speed U_a is higher than the critical speed $U_{\mathrm{cr}} = 0.05(\rho_w - \rho_i)g2r_e/(\rho_w \mathcal{D}_r)$, where $r_e = (3a_r/2)^{1/3} r$ is the effective spherical radius of the frazil ice disks, $\mathcal{D}_r = 2.5 \times 10^{-3}$ is a drag coefficient, $\mathcal{H}$ is the Heaviside function with $\mathcal{H}(x < 0) = 0$ and $\mathcal{H}(x \geq 0) = 1$, and $\rho_w = 1040$ kg m^{-3} is the density of seawater. Note the appearance of the mixed layer depth in the denominator to spread the effect of the frazil ice removal over the whole depth of the lead box. During frazil ice formation, the volumetric rate of grease ice formation per unit length of a lead due to frazil ice emergence at the sea surface is

$$V_l^{f \to g} = R L_o D C. \qquad (4)$$

The shape of the grease ice cover and the rate of its consolidation into sea ice is described in Fig. 2 and appendix A. The frazil ice emergence at the sea surface reduces the depth of the mixed layer by the amount equivalent to the thickness of the newly formed ice; however, we assume it to be constant because of the considered implementation in CICE and any effect of the mixed layer depth change should be accounted for separately.

The last term on the rhs of Eq. (1) describes removal of frazil ice by transportation into the ambient box with the open lead width L_o in the denominator redistributing the frazil ice removal uniformly across the lead box. The process of transportation alters both the lead and ambient boxes, with full equations derived in section 3. We assume that all ice removed through transportation into the ambient box is split proportionally between the grease ice and sea ice areas and deposits on the bottom of the surrounding sea ice uniformly with regard to the sea ice thickness. The volumetric rate contribution to sea ice growth by frazil ice per unit length of one lead is

$$V_a^f = D U_a C. \tag{5}$$

The water temperature is affected by heat transfer and phase change processes, governed by

$$\dot{T} = -w'\left(T_f - T - \frac{H_f}{c_w}\right) + \frac{Q}{D\rho_w c_w} + U_a \frac{T_a - T}{L_o}, \tag{6}$$

where $c_w = 3974\,\mathrm{J\,(kg\,{}^\circ C)^{-1}}$ is the specific heat of water and

$$w' = \kappa(T_f - T)C\frac{\rho_i}{\rho_w}$$

is the volume of water turning into ice per unit time and unit volume of mixture. The term $(T_f - T)$ describes the heating of the supercooled water up to the freezing temperature where ice is produced, while H_f/c_w describes the energy released during ice water solidification. The second term describes the heat flux into the lead box with the net heat flux Q the sum of the surface atmospheric heat flux Q_w and deep ocean heat flux Q_o, while the third term represents heat transport from the ambient box into the lead box. Again, the heat flux is distributed equally over the whole depth of the mixed layer, while the heat transport is over the whole width of the lead box.

Assuming zero salinity of frazil crystals, the following balance holds for salinity

$$\dot{S} = w'S + U_a\frac{S_a - S}{L_o}, \tag{7}$$

where the first term is salt released during water solidification and the second term is the salinity transport from the ambient box into the lead box. Precipitation into and evaporation from the lead have been neglected for this study, though they can play a role in the salinity balance. There is also no explicit consideration of meltwater runoff into leads, although this is

somewhat accounted for through runoff into the mixed layer as a whole. For model simplicity, the mixed layer salinity S_m is prescribed from a dataset (described in section 4a) and the lead and ambient box salinities are balanced with

$$S_m = AS_a + (1 - A)S = A(S_a - S) + S, \tag{8}$$

so that the ambient salinity can be excluded from the salinity balance in Eq. (7), giving

$$\dot{S} = w'S + U_a\frac{S_m - S}{AL_o}. \tag{9}$$

When a lead is formed, the initial lead box temperature is above freezing and the temperature drops to, and typically shoots below, the steady state temperature (Omstedt and Svensson 1984), as frazil ice cannot be produced quickly enough to quench the supercooling. As the frazil ice concentration increases, a steady state is approached. Modeling this process accurately requires solutions for C, S, and T using the coupled system of Eqs. (1), (6), and (9). Because of the complexity of this system, finding evolution of the frazil ice model characteristics analytically is complicated. Furthermore, since the model describes the dynamics of a single lead box, the advantage of numerical implementation of this model on the geophysical scale can be questioned since different leads close and open simultaneously and are at different stages of evolution within one grid cell. Therefore, for our geophysical-scale parameterization, we idealize the process by assuming that frazil ice formation is described by two stages following one another: 1) the lead box temperature decreasing to the steady-state temperature solution where the presence of frazil ice is only accounted for through supercooling of water to an equivalent temperature T_e and 2) the steady state solution.

1) STAGE 1: INITIAL COOLING DOWN OF THE LEAD BOX

During the initial cooling down of the lead box there is no frazil ice and the lead box temperature is given by a reduced version of Eq. (6):

$$\dot{T} = \frac{Q}{D\rho_w c_w} + U_a(T_a - T)/L_o,$$

which, assuming the heat flux and the depth are constant, has the solution

$$T = \left(T_a + \frac{QL_o}{DU_a\rho_w c_w}\right)[1 - \exp(-U_a t/L_o)] + T_0 \exp(-U_a t/L_o),$$

where $T_0 \leq T_a$ is the initial temperature. The lowest temperature that the lead box can reach under stationary forcing is

$$T_{\min} = T_a + \frac{QL_o}{DU_a\rho_w c_w},\qquad(10)$$

which, as will be seen later, is also the temperature given by the steady-state frazil model solution with $C = 0$.

2) STAGE 2: STEADY STATE

During a steady state, the heat released from ice freezing and net heat transport into the box by the warmer ambient water is lost at the surfaces. Similarly, all formed frazil ice is either deposited on top as grease ice or transported into the ambient box. If we define the steady state temperature of the lead box as T_s, then from Eq. (1) we immediately find the amount of supercooling as

$$T_f - T_s = \frac{U_a/L_o + R}{\kappa} \equiv \alpha_1,$$

denoted by constant α_1, allowing us to express the temperature through the salinity as

$$T_s = -\mu S - \alpha_1,\qquad(11)$$

where $\mu = 0.054$ psu °C^{-1} as before. Substituting $T = T_s$ into the heat balance [Eq. (6)], we can express the frazil ice concentration through the salinity

$$C = \alpha_2 + \alpha_3 S, \quad \text{where}$$
$$\alpha_2 = \frac{Q/(D\rho_w c_w) + U_a(T_a + \alpha_1)/L_o}{\alpha_4(\alpha_1 - H_f/c_w)},$$
$$\alpha_3 = \frac{\mu U_a/L_o}{\alpha_4(\alpha_1 - H_f/c_w)}, \quad \text{and} \quad \alpha_4 = \kappa\alpha_1\frac{\rho_i}{\rho_w}.\quad(12)$$

Substituting C into the salt balance [Eq. (9)] yields a quadratic equation for salinity with the solution

$$S = \frac{1}{2}(-\alpha_5 + \sqrt{\alpha_5^2 - 4\alpha_6}), \quad \text{where}$$
$$\alpha_5 = 1 - \frac{U_a}{AL_o}\frac{1}{\alpha_3\alpha_4}, \quad \text{and} \quad \alpha_6 = S_m(1 - \alpha_5).\quad(13)$$

Only the positive root of the quadratic in Eq. (13) is considered, as the negative root gives a negative salinity due to $\alpha_5 = O(10^3)$. Given the lead box salinity S, the frazil ice concentration and water temperature can be found consecutively from Eqs. (12) and (11). We can find the equivalent temperature T_e that describes the same energy state of the lead box without frazil ice as the found solution with ice,

$$T_e = T_s + C\frac{\rho_i}{\rho_w}\left(T_f - T_s - \frac{H_f}{c_w}\right).\qquad(14)$$

Since our mixed layer model does not account for frazil ice directly, this temperature will represent the presence of frazil ice in the lead box. When the equivalent temperature T_e of the steady-state solution is lower than $T_{\min}$, the steady state cannot be attained by the system, and as a result the steady-state solution determines an unphysical $C < 0$; similarly, $C = 0$ if $T_e = T_{\min}$ and $C > 0$ if $T_e > T_{\min}$.

The steady-state solution for mixed layer depth $D = 20$ m and ambient box salinity $S_a = 34.5$ psu is plotted in Fig. 3. It can be seen that despite the nonlinearity of the solution with regard to the ambient temperature T_a and the net heat flux Q, for the range of realistic parameters the nonlinearity is very weak. This is explained by the fact that in the salinity solution the nonlinearity in T_a and in Q arise from the effect of the salt release during water freezing, which is much smaller than the effect of salt transport [$\alpha_4\alpha_3$ versus U_a/AL_o in the definition of α_5 in Eq. (13)]. Since the effect of transport prevails, the solution is clearly nonlinear with regard to the speed U_a. As one could expect, the solution shows higher frazil ice concentrations for higher ambient water temperatures, lower transport speeds, and higher heat loss from the lead box. We have cut off all the curves where the frazil ice concentration becomes negative, implying that such steady-state solution cannot exist, for example, when the ambient water is too warm.

3. Model of the mixed layer

In this section, the two solutions are expanded into a model of the ocean mixed layer in a continuum sea ice climate model. Such a model is not able to explicitly consider the formation and state of individual leads, so we introduce an average representation of multiple leads over a model gridcell area. The length scales associated with multiple leads are defined in section 2 and the fraction of frazil ice producing leads is given by Eqs. (15)–(17). The leads are represented by their area fraction over a grid cell and the temperature of the water within the lead and ambient boxes that are modeled simultaneously by Eqs. (21) and (22). Technical information relating specifically to the CICE model is included in appendix B.

a. Representation of the mixed layer in a large-scale model

If an ocean model includes the mixed layer temperature T_m as a prognostic variable, then, since in our model of a single lead $T_m = A_o T + A_c T_a$, a known T_m does not
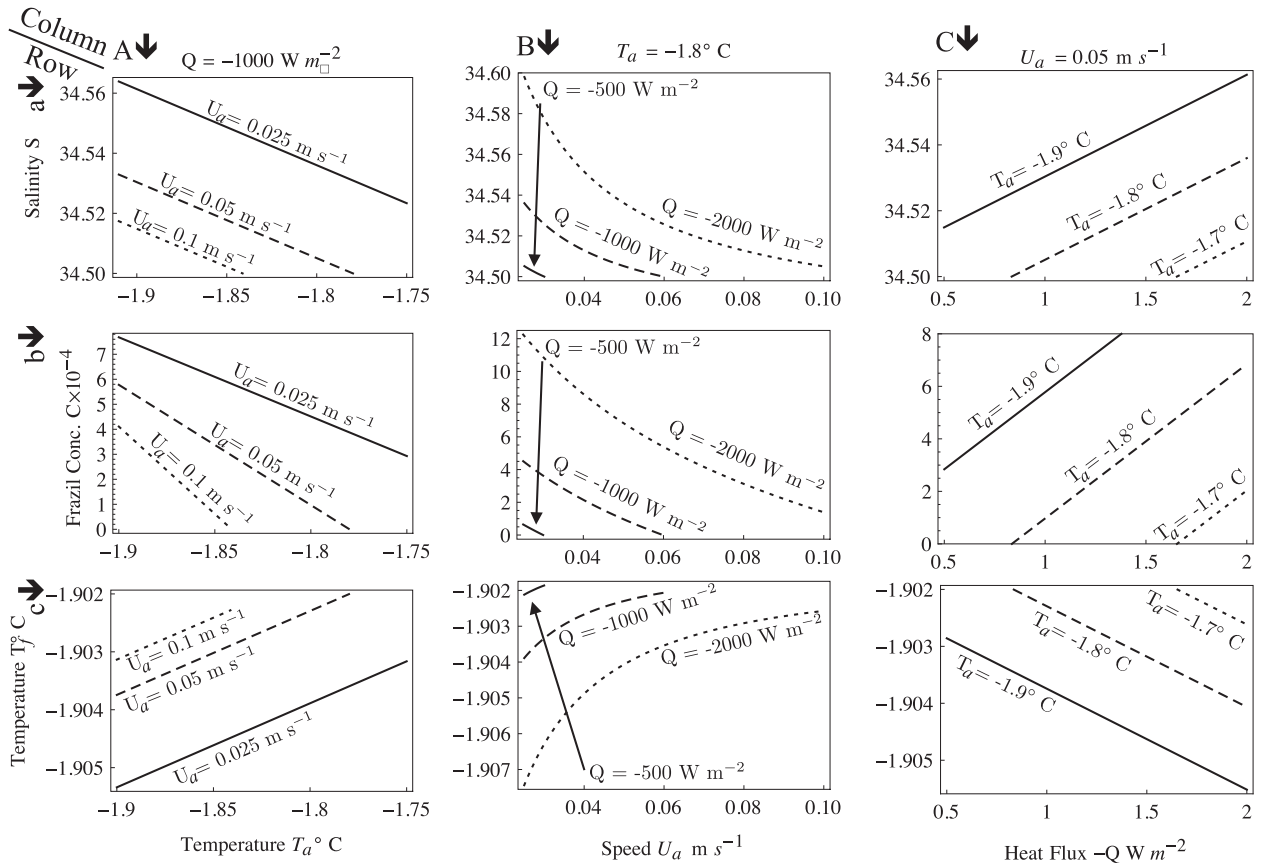
FIG. 3. The steady-state solution for varying parameters: column (A) for varying ambient box temperature T_a and constant Q and U_a; column (B) for varying ambient water speed U_a and constant T_a and Q; column (C) for varying ocean heat flux Q and constant T_a and U_a; row (a) for varying salinity S, row (b) for varying frazil ice concentration C; and row (c) for varying freezing temperature T_f.

uniquely define the lead box and ambient box temperatures T and T_a. Therefore, in our model, rather than having the mixed layer characteristics as prognostic variables, we consider those of the ambient and lead boxes. The single lead box temperature T found by considering the cooling downstage of one lead depends on the time lapsed after the lead formation. While for one lead this time and therefore T can be calculated, on the geophysical scale described by ocean models, there can be different instances of leads at different stages of cooling down or at the steady state, described by only one value: the average temperature of the lead box over all lead instances T_l. In the geophysical-scale context, we therefore redefine $T_m = A_o T_l + A_c T_a$, assuming that the open water fraction A_o and the ambient water temperature and salinity are known and evenly distributed over all lead instances. Considering a grid cell that contains leads that are all cooling down and assuming that they have temperatures that are evenly distributed between the ambient temperature T_a and the minimum temperature of the lead box T_{min} from Eq. (10), which must be

greater than the steady-state equivalent temperature T_e from Eq. (14), we can assign equal probabilities to lead box temperatures during the cooling down stage, finding T_l for leads with no frazil ice formation with

$$T_l = \frac{1}{T_a - T_{min}} \int_{T_{min}}^{T_a} T\, dt = \frac{1}{2}(T_a + T_{min}), \quad (15)$$

where T_a is known from the previous model time step. As T_{min} reaches the limit of T_e, a fraction ξ of the leads within the grid box will start to form frazil ice and will have temperature T_e. The remaining leads of fraction $1 - \xi$ we assume to still have temperatures evenly distributed as before, and by replacing T_{min} with T_e in Eq. (15), their mean temperature is $T_c = (T_a + T_e)/2$. Considering both these fractions, we can write the mean lead box temperature as

$$T_l = \xi T_e + (1 - \xi)T_c. \quad (16)$$

Using Eq. (16), the probability of the frazil ice formation in a lead box can be found from the mean lead box and ambient temperatures with

$$\xi = \frac{T_l - T_c}{T_e - T_c}. \tag{17}$$

The calculated steady-state probability ξ allows us to find the volumetric rates of grease ice formation per unit grid area in the lead and ambient boxes, V_l^g and V_a^g from Eqs. (4) and (5):

$$V_l^g = \xi A_o RDC, \quad V_a^g = \xi D U_a \frac{C}{L}. \tag{18}$$

If all the frazil ice turns into sea ice, then there is a freshwater flux per unit grid area of volume V_f^w out of the mixed layer into the sea ice cover because of frazil ice formation with $V_f^w = (V_a^g + V_l^g)\rho_i/\rho_w$. In this study the salinity of the mixed layer is prescribed, although this flux is important for further study or the implementation with a sea ice–ocean coupled model.

Since the temperatures of lead and ambient boxes are prognostic variables, they are affected by heat exchange at the box's interface. Frazil ice is transported to the ambient box as supercooling, which is then added to the sea ice bottom as deposited frazil ice. Therefore, the integral heat flux from the lead box fraction into the ambient box fraction is Q_a, the mean heat flux over all possible temperature possibilities including that of the steady state with

$$Q_a = \rho_w c_w U_a D (T_l - T_a), \tag{19}$$

since T_l is the mean by definition. Heat transport out of the lead box needs only to be considered for leads in the cooling down stage. The temperature of leads in the steady state is defined by Eqs. (11)–(14), where the heat transport is included within the balance. Therefore, the net heat flux into the lead box fraction from the ambient fraction will then be

$$Q_l = (1 - \xi)\rho_w c_w U_a D (T_a - T_c). \tag{20}$$

b. Mixed layer evolution

The heat flux into the lead boxes from the ambient boxes calculated per unit grid area is Q_l/L. When the fraction of open water excluding grease ice A_o increases by dA_o, then this dA_o comes from the ambient box and adds the ambient water energy into the lead box. When the open water fraction decreases by dA_o, then this dA_o comes from the lead box and removes the lead box energy:

$$\frac{d}{dt}(T_l A_o) = \frac{Q_l}{\rho_w c_w DL} + \frac{Q A_o}{\rho_w c_w D} + \mathcal{H}(\dot{A}_o)\dot{A}_o T_a$$
$$+ \mathcal{H}(-\dot{A}_o)\dot{A}_o T_l,$$

where $\mathcal{H}$ is the Heaviside step function as used in Eq. (3), and since a lead box is positioned under a lead within moving sea ice, the material time derivative d/dt is associated with the moving sea ice. Rearranging the terms, we obtain

$$\dot{T}_l = \frac{Q_l}{\rho_w c_w DLA_o} + \frac{Q}{\rho_w c_w D} + \mathcal{H}(\dot{A}_o)\frac{\dot{A}_o}{A_o}(T_a - T_l). \tag{21}$$

Similarly the heat balance for the ambient box is

$$\frac{d}{dt}(T_a A_c) = \frac{Q_a}{\rho_w c_w DL} + \frac{Q_c A_c}{\rho_w c_w D} + \mathcal{H}(\dot{A}_c)\dot{A}_c T_l$$
$$+ \mathcal{H}(-\dot{A}_c)\dot{A}_c T_a,$$

where $A_c = 1 - A_o$ is the area fraction covered by sea ice and grease ice and Q_c is the net heat flux from the ocean Q_o and through the grease and sea ice Q_i. Rearranging yields

$$\dot{T}_a = \frac{Q_a}{\rho_w c_w DLA_c} + \frac{Q_c}{\rho_w c_w D} + \mathcal{H}(\dot{A}_c)\frac{\dot{A}_c}{A_c}(T_l - T_a). \tag{22}$$

The material time derivative of the ambient box temperature $\dot{T}_a$ is associated with the mixed layer while that of the sea ice and grease ice area $\dot{A}_c$ with sea ice. By neglecting the mixed layer velocity, as in the used version of CICE, a partial derivative instead of full derivative for T_a can be used.

4. Results

a. Standard run configuration

We use CICE version 4.1 described by Hunke and Lipscomb (2010), with modifications as described in appendixes A and B. The model grid is a polar section of a grid with 0.5° resolution with poles rotated to the equator. Apart from the modifications to the frazil ice formation scheme, the model setup is the same as that used by Flocco et al. (2012). The atmospheric forcing set is the National Centers for Environmental Prediction–National Center for Atmospheric Research (NCEP–NCAR) 40-Year Reanalysis Project global dataset (Kalnay et al. 1996). This forcing set was chosen for its good overall performance for surface-level processes in the Arctic (Jakobson et al. 2012), although the radiative fluxes have been shown to be too high because of poor representation of the cloud fraction (Curry et al. 2002; Zib et al. 2012). For the Antarctic the data also perform well at surface levels, although there is a bias for too cold air temperatures in the western Antarctic (Yu et al. 2010) and radiative fluxes that are too high (Vancoppenolle

et al. 2011). The mixed layer model is a slab model as described by Bitz et al. (2012) that is forced by a combined lateral and deep ocean heat flux. This flux is given by climatological monthly means from a Community Climate System Model (CCSM) climate run (b30.009; Collins et al. 2006) smoothed over a 5-day period in order to give a realistic ice state and used as Q_o as in Fig. 1 for the mixed layer. Climatological monthly means are taken from MYO-WP4-PUM-GLOBAL-REANALYSIS-PHYS-001-004 (Ferry et al. 2015) for the mixed layer salinity at depth of 3 m used to prescribe the mixed layer salinity and the ocean current at a depth of 23 m. These data are also used to prescribe the initial ocean temperature. While the ocean current velocities are used to determine ocean drag, the mixed layer temperature is not advected horizontally between grid cells with the ocean current. The ice strength term $C_f = 25$ was tuned to give an Arctic ice thickness similar to that of the Pan-Arctic Ice Ocean Modeling and Assimilation System (PIOMAS) data (Schweiger et al. 2011). The same tuning parameters were used for all the CICE runs, both Antarctic and Arctic and with and without the new frazil scheme. The model was spun up with 10 years of forcing from 1979 to 1989 and then run forward with forcing from 1979 onward, with results from 1980 through 2013 analyzed.

For our standard run we choose $\phi = 10°$, giving the grease ice resistance strength $K_r = 866\,\mathrm{N\,m^{-3}}$ in Eq. (A2) for $\eta = 0.25$. The fixed length of the lead to sea ice structure L is taken as 5 km, so that a 0.9 sea ice concentration will determine a lead width of $L_l = 500\,\mathrm{m}$. The mixed layer depth is fixed as 20 m. The used CICE model does not track the orientation of leads that are necessary for determination of the drag and transport across the leads. Although the Antarctic ice is much less subject to compressive failure, given that the typical small-scale lead intersection angle in the Arctic is roughly 60° (Hibler 2001), for our standard run we somewhat arbitrarily assume that leads are symmetrically positioned at $\phi_l = 30°$ angles with respect to the combined wind and water drag stress direction. There is no quantifiable difference in computational cost between the old and new schemes.

b. Antarctic simulation

While our CICE simulations do a reasonable job of simulating Southern Ocean sea ice, all new frazil and old frazil model runs overestimate the maximum and underestimate the minimum of the Antarctic sea ice area (Fig. 4b). This is true for comparison to both the Bootstrap (Comiso 2000) and NASA Team (Markus and Cavalieri 2000) analysis of SSM/I data with modeled winter ice concentration being too high. The overall sea

ice extent has a good match except in the summer, when the CICE model predicts too little ice (Fig. 4a). The CICE model underestimates the amount of sea ice in the Weddell and Ross Seas. The maximum sea ice area is determined by the area of water cooling down below the freezing point along with sea ice advection and is strongly forced by the mixed layer model and its forcing. Therefore, better data on turbulent heat fluxes from the ocean and heat losses to the atmosphere are required for a better agreement between the models and observations. The minimum sea ice area is determined not only by forcing but also by the model parameters like sea ice albedo. In this work, however, we focus on the impact of the new frazil ice formation model only with the precise tuning of the models and the impact of forcing bias as described in section 4a being outside the scope of this paper.

Example simulations are shown for the CICE model with the new frazil scheme and the old frazil scheme with collection depths of $h_c = 5\,\mathrm{cm}$ (the default value) and $h_c = 30\,\mathrm{cm}$ (which we will now refer to as the tuned old frazil model). The new frazil model was also run with these two depths which, because of the inclusion of the new frazil scheme, only play a role during the beginning stage of sea ice formation in the open ocean. Therefore, the new model has much less sensitivity to this parameter than the old model and was set at the documented default value of $h_c = 5\,\mathrm{cm}$ for the demonstration runs documented here. Frazil and congelation ice are formed for most of the year, with no ice formed in the first 2 months at the height of the melt season. The frazil ice formation rate peaks in May for the old model runs and July for the new model runs (Fig. 4d). The new frazil scheme produces 5 times as much frazil ice as the old scheme with $h_c = 5\,\mathrm{cm}$ and similar amounts to the tuned old scheme. In comparison to the observations presented in section 1, the new and tuned old scheme have greater correlation with frazil ice production at approximately 40% of the total production compared to only 7% for the old scheme with $h_c = 5\,\mathrm{cm}$. Jeffries and Weeks (1992) observed a frazil ice fraction with a mean of 38.5% ± 27%, although from this study and others there appears to be large local and pack-wide variations in the fractions of frazil ice, so there is limited validation available from these datasets. The yearly temporal shape of congelation ice growth is similar for the three example runs: the old scheme with $h_c = 5\,\mathrm{cm}$ produces the most congelation ice, with the new scheme and tuned old scheme having similar rates of formation. The overall rate of ice formation is greatest for the new frazil scheme, with the tuned old scheme close behind and with the old scheme with $h_c = 5\,\mathrm{cm}$ having the lowest combined ice formation rate. This rate of formation has
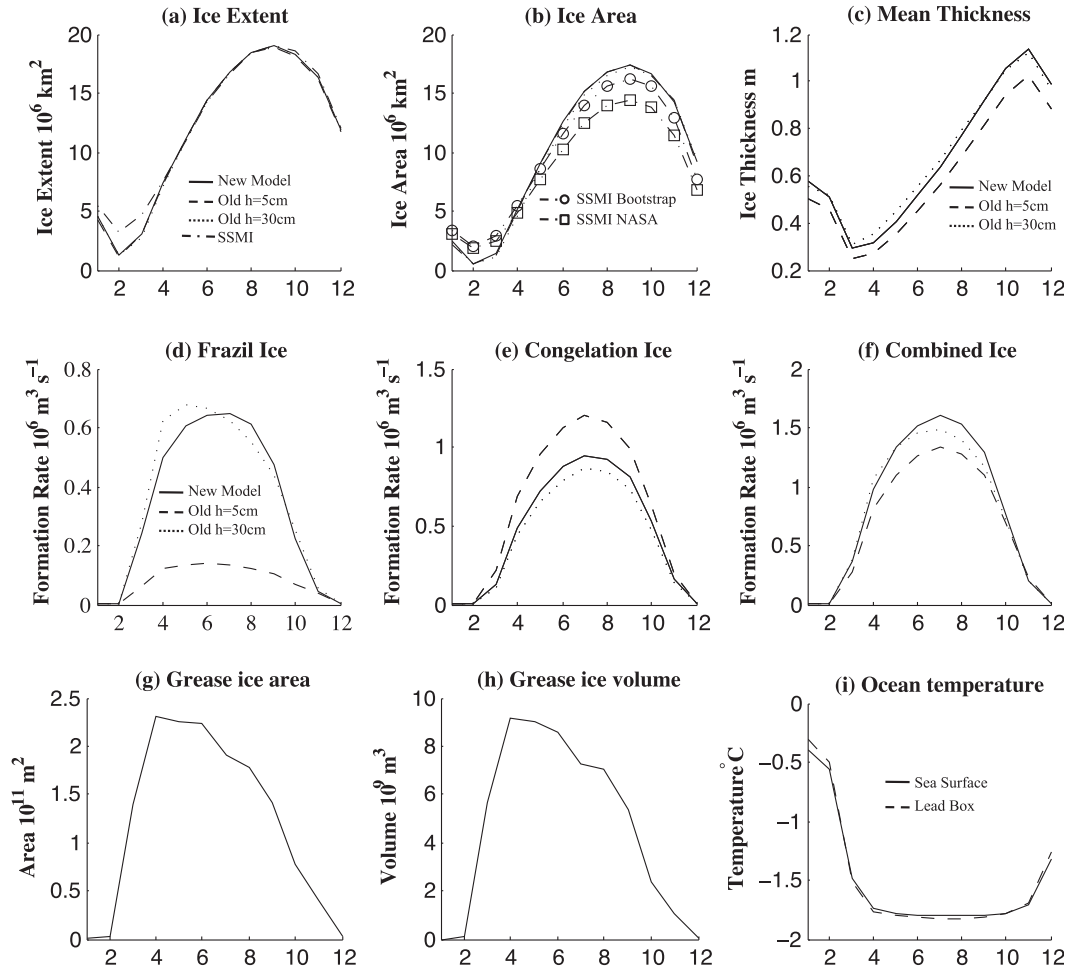
FIG. 4. Monthly means over years 1980–2013 produced by different models over the whole Antarctic: (a) sea ice extent, (b) area including SSM/I observations (dashed–dotted lines) and (c) mean thickness, (d) frazil and (e) congelation ice volumetric formation rates, and (f) the cumulative rate. The solid line is the new model, the dotted line is the old unmodified CICE model with frazil ice collection depth $h_c = 30$ cm, the dashed line is with $h_c = 5$ cm, and the dashed–dotted line is the SSM/I Bootstrap ice concentration from the Bootstrap and NASA teams. Also shown are the (g) grease ice area and (h) volume and (i) ocean temperatures in the new model.

an effect on the overall thickness of the pack, with the new and tuned old scheme having on average sea ice 5 cm thicker than the old scheme with $h_c = 5$ cm (Fig. 4c). There is no significant change in the modeled Antarctic extent, thickness, and ice formation rates with characteristics deviating from the mean by less than 5%. This may be in part because of the atmospheric forcing set, which has the sea ice extent imprinted into it and is unable to respond to changing surface conditions.

For the new frazil model, the grease ice formation follows a similar evolution to the frazil ice with no formation in January and February. The grease ice area and volume reach a peak in April as sea ice quickly forms and then decreases throughout the year (Fig. 4g,h). The average sea surface temperature and lead box temperature

where sea ice is present are plotted (Fig. 4i). The sea surface temperature is close to the freezing point of seawater ($-1.8°$C) for most the year, with the lead box temperature typically $0.02°$C less for this time because of supercooling. During the summer melt season the sea surface temperature increases to around $-0.5°$C, with the lead box temperature typically $0.06°$C higher because of the solar radiation being focused upon the lead box rather than the whole mixed layer.

The spatial characteristics of ice concentration, thickness, and formation rates in the new and old frazil schemes are shown in Fig. 5. The new model is compared with the tuned old model to show the changes the new scheme has on the spatial distributions of sea ice. We present the model characteristics for July (a month of
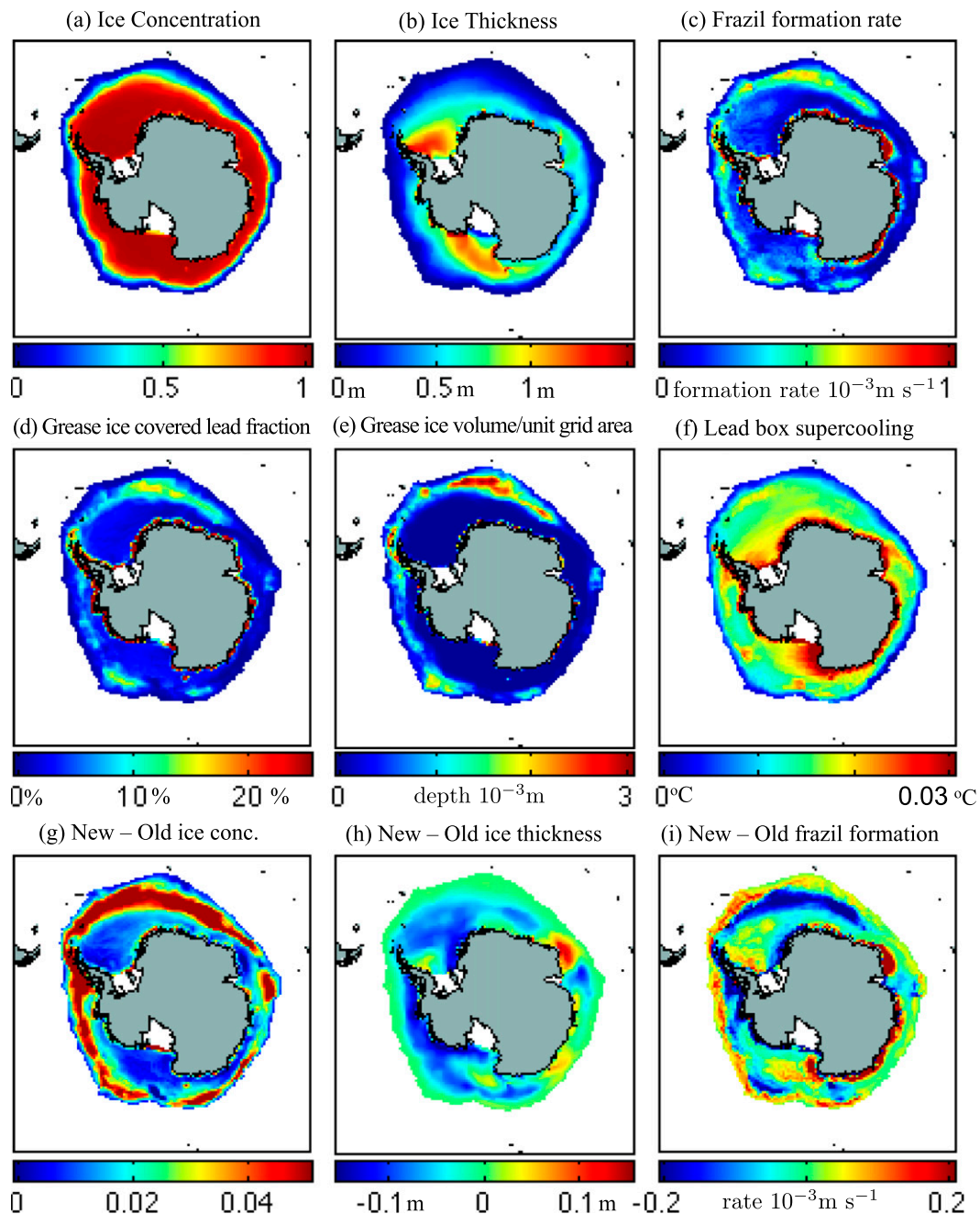
FIG. 5. Antarctic July means from the years 1980–2013 for the new model showing (a) concentration, (b) thickness, (c) frazil ice formation rate, (d) fraction of ice-free (or lead) area covered in grease ice, (e) the volume of grease ice per unit grid cell, and (f) the lead box supercooling. The new and tuned old frazil models are compared (new model minus old model) showing the difference in (g) ice concentration, (h) thickness, and (i) frazil formation rate.

high ice formation) averaged from 1980 through to 2013, showing that the production of frazil and grease ice is in two main areas: low ice concentration regions in the marginal ice zones (MIZs) and in the polynya-like regions next to the Antarctic continent (Fig. 5c–e). Closer inspection of the daily model output reveals that the

pattern of frazil ice formation in the MIZ in both models follows weather systems that open the fragile sea ice cover to expose the open ocean. Frazil ice is then produced as the open ocean, or leads, are refrozen. In the tuned old model this typically takes 2–4 days depending on the scale and persistence of the sea ice deformation

after which frazil ice production will stop. In the new model the frazil formation starts up to a day later because of the initial cooling of the lead box and then will last 1–2 days longer than in the old model.

The polynya-like areas have higher frazil formation rates in the new model where there is a greater fraction of the ice-free areas covered by grease ice, though the volume of grease ice formed is greater in the MIZ. Note that where we mention "polynyas" we refer to leads in the model grid cells next to land or ice shelves. There is no explicit consideration of the mechanics of polynya formation within the model, and the frazil formation scheme assumes that the ice-free areas of the grid cells next to land are arranged into leads evenly spaced by the structure length L throughout the grid cell, as it does with every sea ice grid cell. The model does not consider the dynamics of large open polynyas at the sea ice to land or ice shelf interface, as is often observed in the Laptev (Dmitrenko et al. 2010) or Weddell Seas (Eicken and Lange 1989). The high rates of frazil ice formation in the coastal areas are mechanical in origin. As the modeled sea ice in the grid cell adjacent to land is held still on the cell edge touching land, any sea ice drift in this area causes high rates of stress that will open up new areas of open ocean. This causes high rates of frazil formation until the areas have frozen over. The mechanism of freezing over produces the high fraction of open ocean covered by grease ice in Fig. 5d. This mechanism only happens in grid cells next to land and produces high localized frazil formation rates in both the new and old models.

At the beginning of the ice formation season (March and April), the new frazil scheme produces a lower ice concentration and higher frazil formation rates in the MIZ (not shown), which causes the sea ice extent to advance slightly quicker, though this is not observable in Fig. 4a. In the central pack, however, the new model has a higher ice concentration and the tuned old model has produced thicker ice because of the "head start" given by the unphysical initial collection thickness of 30 cm (see Figs. 5g,h). These differences reduce throughout the freezing season, with the average ice thickness taking the longest to reduce (see Fig. 4c). The mean open water area in such cells undergoing freezing is more than 2 times larger in the new model than in the tuned old model. This is because of new ice collecting as grease ice herding at the edge of the lead rather than as a uniform covering of equal collection depth, which slows down the freezing over of leads. The new model assumes narrow leads in high sea ice concentration areas and wide leads in low concentration areas [$L_l = (1 - A)L$; see section 2a]. For the same frazil ice volume per unit lead area and the same drag stress magnitude, the grease ice thickness will be higher in wider leads as the drag

stress will be integrated over a larger area and smaller in the narrower leads. In contrast, the tuned old model with a constant frazil ice collection depth does not account for this mechanism, even though the spatially averaged characteristics are preserved. By the months of September (not shown) when the models have a similar ice extent, the new model has higher rates of frazil formation in the central pack, producing greater spatial variation in thickness and ice concentration than the old model that has a high rate of ice formation in the MIZ.

c. Arctic simulation

Compared to SSM/I satellite observations from the Bootstrap and NASA team, both old and new frazil models present, on average, a realistic maximum sea ice area and extent (Figs. 6a,b). Spatially, the area of greatest error is in the Greenland and Siberian seas, where the ice concentration is too high. Compared to the PIOMAS product, our modeled maximum sea ice is too thick (Fig. 6c), particularly next to the northern coasts of Greenland and Canada and in the Greenland Sea. PIOMAS, however, does not use a sea ice model as sophisticated as CICE and underestimates sea ice thickness in the Canadian and Alaskan areas (Schweiger et al. 2011). The modeled minimum sea ice extent is too low with an unrealistic spatial variation in sea ice thickness. The error is less when compared to the data from the NASA team. In recent years as the sea ice extent reduces, the model produces a more realistic extent and area, though the rate of reduction is too slow and the sea ice thickness is too thick next to northern coasts of Greenland and Canada and thinning at too slow a rate. Accurately matching the modeled ice state to observations, particularly the recent reduction in summer minimum, would take extensive retuning of the model and consideration of forcing bias and is beyond the scope of this study.

Example model runs were performed for the Arctic with the same parameter values as for the Antarctic. From Fig. 6 it can be seen that again the old frazil model with $h_c = 5$ cm produces too little a fraction of frazil ice: approximately 9%. The new frazil model gives approximately 35% frazil ice fraction, while the tuned old frazil model with $h_c = 30$ cm gives approximately 30%. Eicken et al. (1995) found 61% of undeformed columnar, 9% of deformed ice, and 18% of frazil ice. If we assume that the deformed ice has the same fraction of frazil ice as the undeformed ice, then the overall frazil ice fraction would become 21%. These measurements, however, are from multiyear ice, so the spatial characteristics also need to be considered. The new model Arctic simulation has no grease ice during the summer melt season, as in the Antarctic simulation (Figs. 6g,h). There is a peak
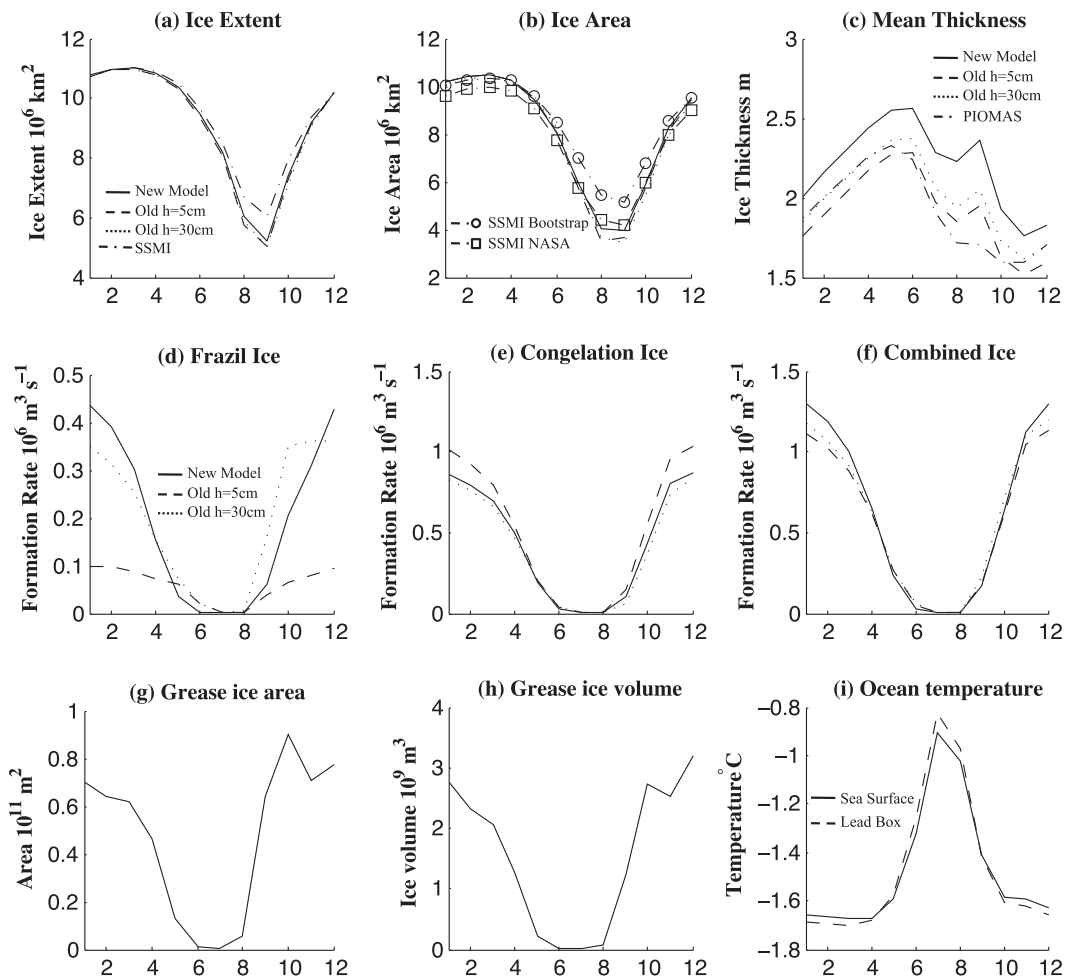
FIG. 6. As in Fig. 4, but including the PIOMAS product (dashed–dotted line).

in grease ice area and volume after the melt season in October and December that then decreases as more grease ice consolidates into sea ice. The sea surface temperature has a similar form to the Antarctic, with the lead box temperature approximately 0.02°C less during the winter and approximately 0.02°C greater during the melt season (Fig. 6i). Despite the ocean temperature forcing coming from a climatology, our March lead box temperature is within the range observed by Morison et al. (1992), which varies between −1.60° and −1.63°C over 3 days of observation in the central pack.

In the areas of the Arctic that have a seasonal ice cover (e.g., Greenland and Barents Seas), the story of the new and old frazil models is similar to that in the Antarctic: the new model has a greater rate of frazil ice formation in areas of higher ice concentration and greater range in ice concentration and thickness at maximum sea ice extent. The frazil ice formation events in the MIZ were similar to those in the Antarctic, with the new model having a

formation period that lasted 1–2 days longer. However, the presence of multiyear ice in the Arctic Ocean requires further consideration. As discussed previously, the method of grease ice herding gives a high fraction of open ocean and greater rate of frazil ice formation in high ice concentration areas in the new model compared to the old model. As rates of congelation ice formation are similar in both old and new models, the central Arctic sea ice pack in the new model has a higher cumulative rate of ice formation in the fall and winter. This higher rate of formation results in a significantly thicker sea ice thickness (up to 0.5 m, see Fig. 7h) between the Bering Sea and Fram Strait, which is the area associated with multiyear sea ice. A thicker sea ice cover takes longer to melt, resulting in the minimum sea ice extent and area in the new model being higher than in the old model, which matches closer to SSM/I observations (Figs. 6a,b), although the model has not been retuned to fit observations and we have not considered any forcing bias when making this
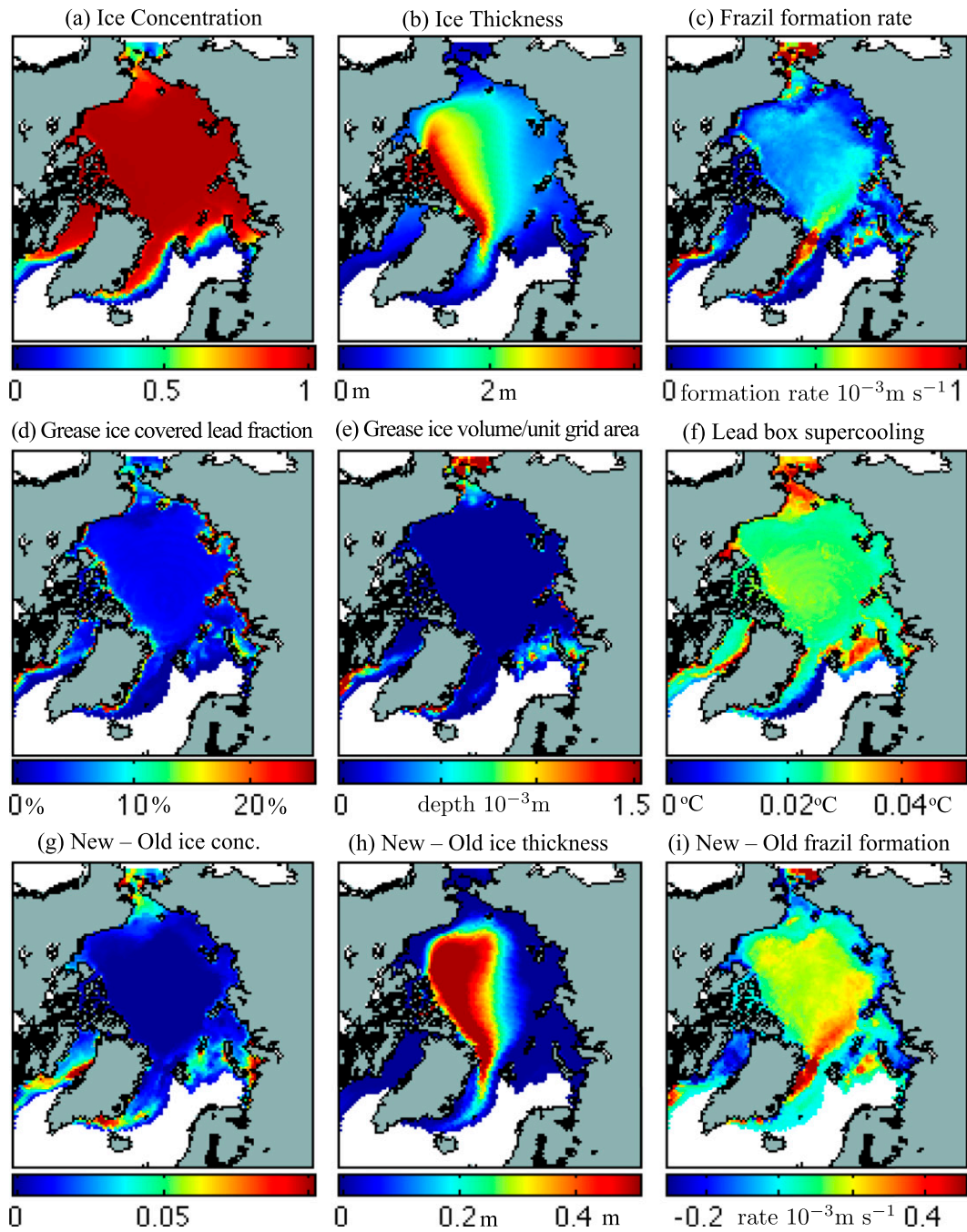
FIG. 7. As in Fig. 5, but for Arctic December means from the years 1980–2013.

comparison. The old model has similar ice thicknesses in the central pack when using both collection thicknesses (5 and 30 cm), showing that the tuning of this parameter will only change the rate of frazil ice production in the marginal seas. The observations of Eicken et al. (1995) discussed above are from a study of level multiyear ice with measurements taken in the central ice pack. The old model with both collection thicknesses has less than 3%

frazil contribution in the central pack. Despite the tuning of the collection thickness to match the contribution of frazil ice formation averaged over the entire ice cover, the old model still neglects the process of frazil ice growth in the central pack and overestimates its contribution in the MIZ.

The lower sea ice extent and greater area of open ocean in the old model gives a higher rate of frazil
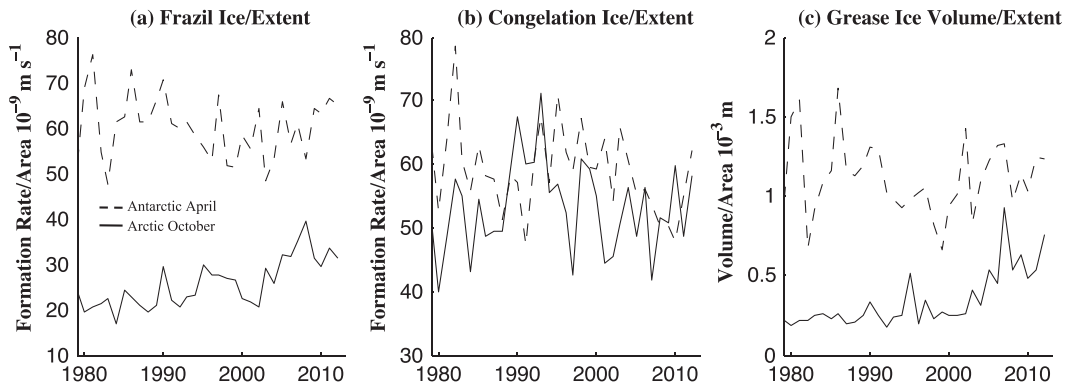
FIG. 8. The changing rates of ice formation in the Arctic and Antarctic over years 1980–2013: rates of (a) frazil and (b) congelation ice formation and (c) grease ice volume weighted by sea ice extent. The example rate is for the Arctic in October (solid line) and the Antarctic in April (dashed line). There has been an increase in the frazil and grease ice production in the Arctic since 2000.

formation in the September and October, allowing it to catch up with the new model (see similar ice concentrations in Fig. 7g) after which the sea ice cover has filled the Arctic Ocean with reduced areas of MIZ in the Greenland, Labrador, and Barents Seas. As the old frazil model's frazil ice production is concentrated in the MIZs, its overall frazil production rate then drops below that of the new model. As with the Antarctic simulations, there are polynya-like areas next to the coast where there is an increased frazil ice formation rate in both models. Because of the intricately shaped coastal geography of the Arctic Ocean, the same mechanism gives increased frazil ice formation in the Fram Strait and Barents Seas for both models (Fig. 7c). The frazil ice production in the new model is further increased in these areas (Fig. 7i), with the Barents also having a high rate of supercooling and grease ice production (Figs. 7e,f).

d. Comparison of Arctic with Antarctic simulations: The role of the MIZ

The results from the new frazil scheme show differences between the state of the Antarctic and Arctic sea ice cover. Figure 8 shows the rate of ice formation averaged over the total ice extent in the Arctic and Antarctic. The Arctic data are taken from October and the Antarctic data from April, the months of greatest grease ice formation per unit area. The model results show that the location and extent of the MIZ has an effect on the state of the ice cover. The rate of congelation ice formation, which is not heightened in the MIZ, is similar for both the Arctic and Antarctic. The rates of frazil and grease ice formation differ. Before 2000 the Arctic summer minimum extent in the new model typically filled the majority of the Arctic basin, resulting in a low

extent of MIZ for the beginning of the new ice formation season. As the summer minimum extent has decreased since 2000, the Siberian Sea has often become ice-free in the summer. This has resulted in a large MIZ that can stretch from the Fram Strait to the Bering Strait. In contrast, the Antarctic has a large extent of MIZ circumscribing the pole throughout the year. As the MIZ is the area of greatest frazil and grease ice formation, the Antarctic has, up to 2000, had a significantly higher rate of frazil formation and grease ice volume per unit area of sea ice cover than the Arctic. Since 2000 the Arctic extent averaged rates of frazil formation and grease ice volume have increased, with the grease ice volume becoming similar to the Antarctic (Fig. 8c). This increase, however, is not experienced throughout the Arctic ice formation season, as by December the sea ice cover has again filled the Arctic basin, reducing the extent of the MIZs and thus the rate of frazil production and grease ice volume.

e. Sensitivity studies

Here we investigate the sensitivity of the new ice formation parameterization to the chosen model parameters. The lead structure length L_l and angle between the lead and the drag stress direction on the grease ice θ_l represent a distribution of leads of different sizes and orientations that we have reduced to arbitrarily chosen values. We have chosen values that are theoretically consistent but are poorly constrained by observations. The lead width L_l is particularly important as it appears in the equations of frazil ice formation (section 2), mixed layer development (section 2), and grease ice shape (appendix A). Changing the grease ice resistance K_r affects the rate of lead refreezing and proposed formulation of stress on grease ice in Eq. (A3).
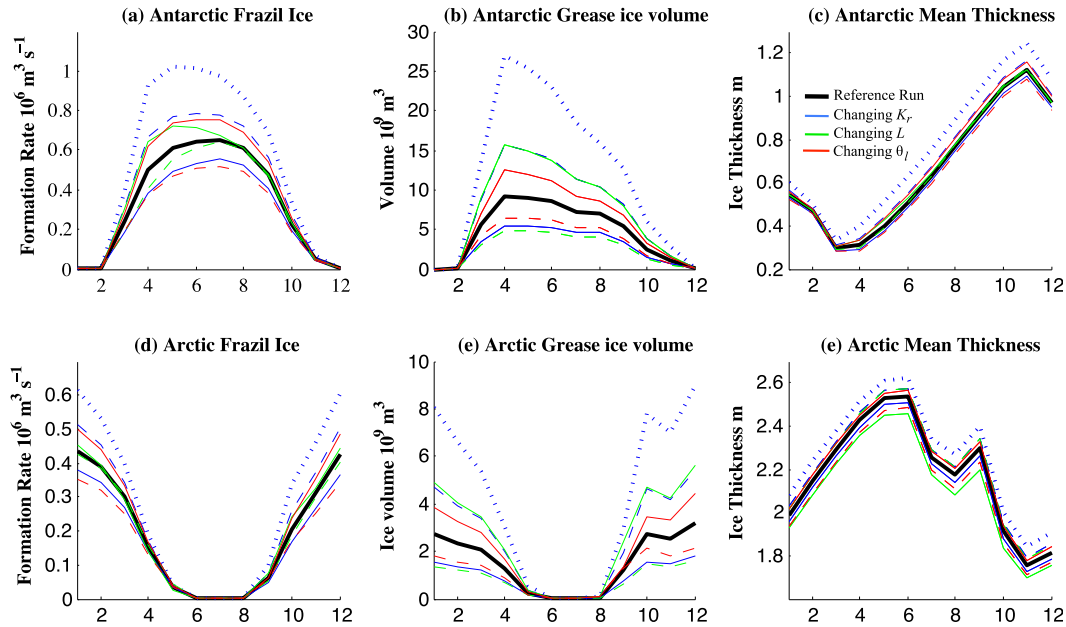
FIG. 9. Sensitivity of the new frazil model to model parameters. The reference run is shown in black compared to changing grease ice resistance K_r in blue, lead–sea ice structure length L in green, and the angle between leads and the drag on grease ice θ_l in red. Each parameter is changed by a factor of 2 (solid line) and 0.5 (dashed line), with K_r further changed by a factor of 0.25 (blue dotted line).

A higher grease ice resistance K_r leads to larger grease ice area and thinner grease ice, so that the lead freezes over faster and the frazil ice formation rates become lower (solid blue line in Figs. 9a,d). A smaller angle of the lead reduces the drag stress projection perpendicular to the lead, which has the same effect as increasing K_r, as they both appear as a ratio in Eq. (A1). A smaller lead width L_l, which is proportional to L, implies a smaller integral drag force on the grease ice and therefore a thinner grease ice layer, leading to a faster freezing over of the lead. From the grease ice model Eq. (A6), by considering the simplest case of all grease ice fitting into the lead, $h_{\min} = 0$, and using $V^g \propto L$, we obtain $A_g = L_g/L \propto (K_r/L)^{1/3}$. In this simplified case, the effect of varying one of the parameters (K_r, L) is analogous of varying the other by the reversed factor, which can be seen in Figs. 9b and 9e, where the solid blue line is aligned with the dashed green line and vice versa. From this result, one would expect a similar relation for frazil ice formation (e.g., increased L gives increased frazil ice formation), though the simulations (Figs. 9a,d) show that frazil ice formation is more sensitive to the grease ice resistance strength K_r and to the lead angle θ_l than it is to the lead–sea ice element length L. This is a result of more complex interactions in the model; for example, decreasing of L for a fixed transport speed will also increase the effect of fluxes between the lead and the sea ice and will therefore increase the volume of frazil ice

transported from the lead box to deposit on the sea ice bottom, which will reduce the amount of frazil ice in the lead and the speed of lead freezing.

The simulations with a greater volume of grease ice and greater frazil formation rates give on average a thicker sea ice cover (Figs. 9c,d). This change is greatest for K_r reduced by a factor of 0.25. This scenario was considered to show the implications of weighting the applied stress on grease ice by the grease ice fraction η. The reduction of K_r by a factor of 0.25 is analogous to replacing η^2 with η in Eq. (A3). The lower strength allows increased grease ice herding, which keeps leads open for longer, giving greater frazil ice formation. The increased herding also causes more grease ice to be deposited onto the existing sea ice. Both processes result in a thicker sea ice cover.

5. Concluding remarks

A new parameterization of frazil and grease ice formation has been developed for incorporation into a climate model sea ice module. The parameterization divides the subgrid-scale mixed layer into a supercooled part under a lead and a part under sea ice cover. Vertical uniformity in the mixed layer is assumed for frazil ice formation characteristics. The temperatures in these mixed layer constituents are found through heat exchange at the top and bottom surfaces of the mixed layer

as well as between the constituents themselves through water exchange during opening and closing of leads. The mean temperature under the lead part of the grid cell represents the temperature of the new leads cooling down and old leads producing frazil ice in assumed steady state. Given the mean lead water temperature found from the solution of the heat balance equation, and the known steady-state solution, the probability of leads producing frazil ice can be found, determining the grease ice formation rate. For the known volume of grease ice, its thickness distribution is determined, similar to Smedsrud (2011), by balancing granular resistance with the air and ocean drag, with a simple correction to account for grease ice being a mixture of ice and water (which could be the subject of future study). Grease ice is herded onto sea ice if its thickness is larger than that of sea ice, for example, because of strong wind or significant reduction in open water areas due to convergence. As heat is lost from the grease ice, its seawater fraction freezes and the corresponding area of sea ice of the same thickness as the grease ice is transferred to the sea ice. Frazil ice swept out of the lead is added to the sea ice bottom. The mixed layer depth in the model was held constant at 20 m, whereas it is observed to be variable (Markus 1999).

Coupling of our frazil and grease ice model within CICE to a well-mixed but variable-depth mixed layer model such as Petty et al. (2014) would be computationally straightforward using existing methods. Coupling to a vertically resolved mixed layer model, such as in a primitive equation ocean model, however, would require some care: a decision must be reached as whether to include frazil ice in the sea ice or ocean model components, to which there are pros and cons for each option. Keeping frazil ice inside the sea ice model will be computationally simple with the mixed layer properties diagnosed from the ocean model and keeping our distinction of lead and ambient boxes. Including frazil ice in the ocean model is more general and powerful (e.g., latent heat polynyas) but computationally more demanding.

The inclusion of the new frazil ice formation scheme increases frazil ice production in high ice concentration areas, relative to the existing schemes, which treat the open water fraction in a high ice concentration central ice pack in the same way as the open water fraction in ice-free and marginal seas. The existing CICE parameterization precipitates new frazil ice into a uniform thin layer, whereas our new model herds the frazil ice as grease ice against the existing sea ice. In the new scheme, the grease ice thickness depends on the air and ocean drag and can be as thick as the existing sea ice, with the grease ice covering a smaller area than in the existing CICE scheme and keeping the lead open. Lead refreezing is slower when using our new parameterization and the continued presence of open water allows for greater frazil ice production. The new scheme process produces greater spatial variation in Antarctic ice concentration and thickness (Fig. 5) and thicker multiyear sea ice in the central Arctic (Fig. 7). The frazil formation scheme is also important in areas where the sea ice cover is mechanically deformed, such as adjacent to coastlines and in the Fram Strait. In these areas there are high internal stresses in the sea ice that can fail to produce areas of open ocean. The presence of open ocean causes high rates of frazil ice formation in both new and old frazil treatments, with the new model having rates of frazil growth that are 50% greater than the previous treatments.

The new model frazil ice formation rate is affected by the grease ice resistance strength and the angle between the leads and the direction of the drag force on the grease ice. These affect the grease ice area and thickness; for example, a higher-resistance strength implies a larger grease ice area and a smaller grease ice thickness, so that the open water area freezes faster and less frazil ice originated sea ice is produced. The sensitivity to the lead width is smaller because of a negative feedback with other effects of the lead width, such as the mixing rate between the lead water and the water under the sea ice.

While the original model can be retuned in order to produce a similar average fraction of frazil ice, the new model's collection thickness is dynamically calculated, allowing for a larger collection thickness in large leads, whereas the old model assumes it to be equal for wide and narrow leads. Retuning the old frazil scheme does not give the same spatial pattern of frazil ice formation as the new frazil scheme, as discussed above. We compared the new frazil parameterization to the existing CICE scheme with two different collection depths: the default model value of $h_c = 5$ cm and a higher value of $h_c = 30$ cm. The higher value was used to give comparable total frazil formation rates between the new and old models over the entire polar region, although the value is unphysically high (Eicken and Lange 1989). The collection depth h_c relates to the observed thickness of new ice found in marginal seas, and the higher value causes the model to produce thicker sea ice and lower ice areas during the first months of ice production in the Antarctic (Fig. 5). When comparing the models to observations, all the Antarctic runs produced higher sea ice areas in the winter and lower areas in summer. There was little difference between the models as the sea ice area is more sensitive to processes other than the new frazil formation scheme, for example, basal melting. For the Arctic, however, the new frazil scheme had an

impact on the sea ice area and thickness. The new model, by the process discussed above, produces multiyear sea ice that is over 0.5 m thicker than the old model. The thicker ice was able to survive the summer melt with approximately 10% greater sea ice area, which was a better fit with summer observations.

The significance of the new frazil and grease ice formation scheme is connected with the extent of the MIZ. During the recent post-2000 reduction in summer Arctic sea ice extent, a MIZ is able to form north of Siberia, comparable in extent to the Antarctic MIZ. As there is a greater rate of frazil and grease ice formation within the MIZ, our simulations show that the relative amounts of granular ice in the Arctic and Antarctic are now similar during the first months of the ice formation season. The volume of grease ice weighted by the overall extent increases for the Arctic from 0.2×10^{-3} m to 0.7×10^{-3} m and is now comparable to the Antarctic, which has a value of 1×10^{-3} m (see Fig. 8). In the inclusion of our new frazil formation scheme allows for a future sea ice model to track the fraction of sea ice that is columnar or granular in origin. This may play a role in the changing state of the Arctic sea ice cover.

APPENDIX A

Grease Ice

a. Grease ice model and redistribution

If the grease ice volume excluding water $V_{(g)}$ is known per unit grid area, then the grease ice volume in the lead of the whole lead–sea ice element will be $V_{(g)}L$. As ice typically constitutes only a $\eta = 0.25$ fraction of grease ice (Martin and Kauffman 1981; Smedsrud and Skogseth 2006; De la Rosa and Maus 2012), while the rest is seawater, the whole grease ice volume will be $V = V_{(g)}L/\eta$. Smedsrud (2011) developed a model for the steady-state spatial distribution of grease ice in a lead or polynya, where the ocean and water drag are balanced by granular resistance, similar to a model of pancake ice herding by waves (Dai et al. 2004). This model calculates the thickness of grease ice h by

$$\frac{dh^2}{dx} = \frac{\tau_c}{K_r} \equiv \zeta, \qquad (A1)$$

where τ_c is the cumulative stress on grease ice from water and air and K_r of $O(100)$ N m^{-3} is associated with granular resistance by

$$K_r = \frac{1}{2} \frac{1 + \sin\phi}{1 - \sin\phi} \eta \rho_g g \left(1 - \frac{\rho_g}{\rho_w}\right), \qquad (A2)$$

where ϕ is an internal friction angle and $\rho_g = \eta\rho_i + (1 - \eta)\rho_w$ is the grease ice density. Note that $\phi = 0$, $\eta = 1$ describes a balance between the water and air drag and the hydrostatic pressure gradient. For this model of grease ice formation, we must consider the stress on grease ice τ_c in relation to the applied stress on sea ice as given by the CICE model τ. Here we propose that the stress on grease ice applies only to the ice fraction. As the applied stress is over a given area of grease ice, we define the relationship

$$\tau_c = \eta^2 \tau \qquad (A3)$$

in Eq. (A1) to give a value for the stress on grease ice. This new equation is investigated in the sensitivity studies (section 4e). Note that this formulation gives the limit $dh^2/dx \to 0$ as $\eta \to 0$. If the drag stress is along the x axis, then h is given by

$$h = \sqrt{h_{\min}^2 + \zeta x}. \qquad (A4)$$

If L_g is the grease ice span as shown in Fig. 1, then the total volume of grease ice V is given by

$$V = \int_0^{L_g} h \, dx = \frac{2}{3\zeta}[(h_{\min}^2 + \zeta L_g)^{3/2} - h_{\min}^3], \qquad (A5)$$

which can be rearranged to give

$$L_g = \frac{1}{\zeta} \left[\left(\frac{3\zeta V}{2} + h_{\min}^3 \right)^{2/3} - h_{\min}^2 \right]. \qquad (A6)$$

If the found grease ice span is larger than the lead width L_l, then all the grease ice will not fit into the lead, and the grease ice span will be determined by the lead width, $L_g = L$, and $h_{\min}$ at the upwind lead edge from Eq. (A6) (see Fig. 2). This solution will, however, only be valid if the maximum grease ice thickness is smaller than the sea ice thickness h_i; otherwise, part of the grease ice will be swept over and under the sea ice and the grease ice volume in the lead will reduce. This is important if there is strong wind or convergence that significantly reduces the lead width, so that the grease ice cannot be accommodated in the lead anymore. To account for this scenario, it first is necessary to find the maximum grease ice volume that can be accommodated by the lead and then

compare it with the existing grease ice volume. If the maximum accommodated volume is larger, then all grease ice is accommodated by the lead. Otherwise, the grease ice volume in the lead will be the maximum accommodated grease ice volume, while the remaining grease ice of volume V_+ will be evenly distributed over the sea ice area. To find the maximum accommodated grease ice volume, we take the maximum grease ice thickness as $h = h_i$ in Eq. (A4), so that putting $h_{min} = 0$ will give L_{max} the unobstructed grease ice span (as shown in Fig. 2a) to be

$$L_{max} = \frac{h_i^2}{\zeta},$$

determining the corresponding grease ice volume,

$$V_{max} = \frac{2}{3\zeta}(\zeta L_{max})^{3/2}.$$

If L_{max} is larger than the lead width L_l, then the grease ice will be obstructed from the upwind direction, and we have to take the grease ice span as L_l (Fig. 2b). This will determine the minimum grease ice thickness as

$$h_{min} = \sqrt{h_i^2 - \zeta L_l}$$

and the corresponding maximum accommodated grease ice volume from Eq. (A5). Any excess grease ice is redistributed evenly over the existing sea ice.

As in numerical models, there are different ice thickness categories described by different h_i, and the grease ice model must take this into account. In our lead–sea ice structure, the ratio of the ice width L_i to the width of the whole lead–sea ice structure L fully represents the sea ice fractional area. To describe the presence of different sea ice thickness categories, we consider an idealized situation in which sea ice thickness is uniform perpendicular to the lead while along the lead the sea ice is split into different thickness categories indexed by j according to their fractional area A_j/A, where A_j is the fraction of ice category j. In this case, the sea ice categories form bands perpendicular to the lead, and the grease ice volume in the lead is the volume per unit width of a band of a particular category. The grease ice volume V_j, grease ice area fraction $A_{g,j} = (L_g A_j)/(LA)$ in the lead, and grease ice volume that overrides and underrides the sea ice V_{j+} are found for all sea ice thickness categories per unit width using Eq. (A5) and onward. The thickness of ice uniformly deposited over the sea ice of a category j is $\eta V_{j+}/L$. The resulting grease ice volume and area are then found by summing over the j indices as the averages

$$V = \frac{1}{A}\sum_{j=1}^{N} V_j A_j, \quad A_g = \frac{1}{A}\sum_{j=1}^{N} A_{g,j}A_j, \quad (A7)$$

where there are N ice thickness categories.

b. Grease ice consolidation

We assume that the heat flux at the air–grease–ice interface is $(1 - \eta)$ times of that of the open ocean–air interface, and all the heat flux is used either to convert grease ice into sea ice or to melt it. We assume that freezing occurs only laterally, so that new sea ice of thickness h_g is produced. The grease ice enthalpy per unit volume of grease ice is q_g and is that of fresh ice and water at the freezing temperature:

$$q_g = (1 - \eta)\rho_w c_w T_f \frac{\rho_i}{\rho_w} + \eta\rho_i(c_w T_f - H_f),$$

where the enthalpy of water is assumed to be zero at 0°C and the factor ρ_i/ρ_w accounts for the part of seawater being squeezed out as it expands during freezing.

New ice formed at the freezing temperature has an enthalpy q_i derived from the specific heat of the ice (Ono 1967), where it is assumed that the new ice has the maximum, undrained salinity S_{max} determining the sea ice melting temperature as $T_{melt} = -\mu S_{max}$ (Schwarzacher 1959):

$$q_i = -\rho_i\left[c_i(T_{melt} - T_f) - L_0\left(1 - \frac{T_{melt}}{T_f}\right) - c_w T_{melt}\right],$$

and S_{max} is taken as 3.2 psu to correspond to the maximum salinity at the sea ice bottom used in CICE.

In freezing ($Q < 0$) all heat lost by the grease ice area is used to freeze a fraction of grease ice of full thickness $h_{g,j}$ [from Eq. (A4) with $x \to L_l$ or L_{max}], so that the rate of area transfer from grease ice to new ice is

$$\frac{da_{g,j}}{dt} = \frac{Q a_{g,j}}{h_{g,j}(q_i - q_g)}. \quad (A8)$$

Note that after the sweeping of grease ice over the sea ice, grease ice thickness is associated with the sea ice thickness, $h_{g,j} = h_j$. In the case of the grease ice being thinner than the adjacent sea ice, that is, $h_{g,j} < h_j$, the consolidated grease ice may belong to a lower sea ice category. In case of melting $Q > 0$, we assume the absorbed heat goes into melting of grease ice only and heating the meltwater up to the lead box temperature so that rate of loss of grease ice area is

$$-\frac{da_{g,j}}{dt} = -\frac{Q a_{g,j}}{h_{g,j}\eta\rho_i[c_w(T_f - T_l) - H_f]}. \quad (A9)$$

APPENDIX B

Implementation of the new parameterization into CICE

CICE is a widely used sea ice climate model [see Hunke and Lipscomb (2010) for more details]. Incorporation of our new frazil and grease ice parameterization into the CICE sea ice model requires adding three more tracers: the grease ice volume per unit grid area, the lead box temperature T_l, and the cumulative sea ice and grease ice fraction A_c, which, along with the existing tracers of the mixed layer temperature (now the ambient box temperature) and salinity T_a and S_m and sea ice fraction A, define the processes within the mixed layer as described in section 3. Tracking A_c is necessary to determine $\dot{A}_o$ and $\dot{A}_c$ in the balance of heat in the lead and ambient boxes, Eqs. (21) and (22). The three new tracers are advected horizontally between the model grid cells along with the sea ice area. This is in contrast with the ambient box temperature T_a that remains stationary to be consistent with the ocean forcing.

For comparison with the unmodified CICE model, the reader is reminded that the unmodified model does not explicitly distinguish frazil ice formation in leads. Frazil ice is allowed to form at the ocean surface wherever sea ice is not present. This results in the same method of frazil ice formation in leads as in the open ocean. Frazil ice is allowed to collect at the surface of the ocean as thin sea ice at a specified collection depth h_c. The amount of frazil ice that collects is determined by a thermodynamic balance between the ocean surface temperature and its freezing point. The formation of congelation ice in modified and standard CICE models is the same; however, the new model considers the characteristics of the ambient box rather than those of the mixed layer as a whole.

At a time step in our new scheme, first the atmosphere and ocean drag across the lead and the mean advection speed across the leads (assumed to be symmetrically positioned around the cumulative drag τ direction) are calculated. Then, since the grease ice volume is known, it is updated through adding the frazil ice in the ambient box (represented through supercooling) positioned under the grease ice area taken from the previous step. The rest of the ambient box frazil ice is added to the sea ice bottom. For the known ocean and water drag stresses, ocean temperature, and sea ice area, a new grease ice area is calculated using Eq. (A7), and the grease ice volume is updated, as some grease ice can over- and underride the sea ice. The under- and overridden ice is added to the model's sea ice thickness distribution, while the new sea ice formed through freezing of the grease ice, as calculated by Eq. (A8), is added to sea ice

categories. As this leads to a change in the cumulative sea ice and grease ice fraction, along with other changes to the sea ice fraction from the rest of the CICE model, the corresponding water energy is exchanged between the lead box and the ambient box, as in the last terms in Eqs. (21) and (22) using the cumulative sea ice and grease ice water fraction from the previous time step. This determines a new open water fraction, and we calculate the equivalent temperature of the steady-state solution for the frazil ice formation using Eq. (14). Comparing this equivalent temperature with the lead box temperature evolving in time from the previous time step, we can find the probability of the steady-state solution ξ from Eq. (17) and the heat flux between the lead and ambient boxes. With the new lead box and ambient box temperatures calculated from Eqs. (21) and (22), the grease ice volume in the lead is updated with the deposited frazil ice using Eqs. (18). The new values are then advected laterally between model grid cells along with the sea ice drift velocity for the next time step.

For simplicity, the seawater freezing temperature is calculated given the mean mixed layer salinity ignoring the difference in salinities between the ambient box and the lead box. The lead box salinity is explicitly considered only when calculating the steady-state temperature for Eq. (14). Note that in CICE we calculate the diagnostic frazil ice formation rate, salinity, and freshwater fluxes only when grease or frazil ice are added to sea ice through grease ice solidification or frazil ice deposition to the sea ice bottom rather than when water becomes frazil or grease ice. For this case, the melting of grease ice does not add to freshwater fluxes. Moreover, the ice obtained through the freezing of seawater contained within grease ice is also counted as frazil ice in its origin; therefore, the frazil ice volumetric rate formation also includes granular ice. The air drag on the grease ice is taken as it is calculated for the sea ice, and the water drag on the grease ice is calculated using a standard quadratic law with the drag coefficient 5.36×10^{-3}, consistent with Steiner (2001). The grease ice model applies only when there is already sea ice present to ensure grease ice herding against it. When frazil ice forms in ice-free water, then we use the old model packing the formed frazil ice into a layer of collection ice thickness of h_c taken to be 5 cm, as in the present version of CICE used for simulating the Arctic.

REFERENCES

Allison, I., and S. Qian, 1985: Characteristics of sea ice on the Casey region. ANARE Research Notes 28, Australian Antarctic Data Centre, 47–56.

Bauer, J., and S. Martin, 1983: A model of grease ice growth in small leads. *J. Geophys. Res.,* **88,** 2917–2925, doi:10.1029/JC088iC05p02917.

Biggs, N. R. T., M. A. Morales Maqueda, and A. J. Willmott, 2000: Polynya flux model solutions incorporating a parameterization for the collection thickness of consolidated new ice. *J. Fluid Mech.,* **408,** 179–204, doi:10.1017/S0022112099007673.

Bitz, C. M., K. M. Shell, P. R. Gent, D. A. Bailey, G. Danabasoglu, K. C. Armour, M. M. Holland, and J. T. Kiehl, 2012: Climate sensitivity of the Community Climate System Model, version 4. *J. Climate,* **25,** 3053–3070, doi:10.1175/JCLI-D-11-00290.1.

Clarke, D. B., and S. F. Ackley, 1984: Sea ice structure and biological activity in the Antarctic marginal ice zone. *J. Geophys. Res.,* **89,** 2087–2095, doi:10.1029/JC089iC02p02087.

Collins, W. D., and Coauthors, 2006: The Community Climate System Model version 3 (CCSM3). *J. Climate,* **19,** 2122–2143, doi:10.1175/JCLI3761.1.

Comiso, J., 2000: Bootstrap sea ice concentrations from Nimbus-7 SMMR and DMSP SSM/I-SSMIS, version 2. Subset used: 1990–1999, National Snow and Ice Data Center, accessed 1 February 2014, doi:10.5067/J6JQLS9EJ5HU.

Curry, J. A., J. L. Schramm, A. Alam, R. Reeder, T. E. Arbetter, and P. Guest, 2002: Evaluation of data sets used to force sea ice models in the Arctic Ocean. *J. Geophys. Res.,* **107,** 8027, doi:10.1029/2000JC000466.

Dai, M., H. H. Shen, M. A. Hopkins, and S. F. Ackley, 2004: Wave rafting and the equilibrium pancake ice cover thickness. *J. Geophys. Res.,* **109,** C07023, doi:10.1029/2003JC002192.

Daly, S. F., 1994: Evolution of frazil ice in natural water bodies. *International Association for Hydraulic Research Working Group on Thermal Regimes: Report on Frazil Ice,* Special Rep. 94-23, 11–17.

De la Rosa, S., and S. Maus, 2012: Laboratory study of frazil ice accumulation under wave conditions. *Cryosphere,* **6,** 173–191, doi:10.5194/tc-6-173-2012.

Dmitrenko, I. A., and Coauthors, 2010: Observations of super-cooling and frazil ice formation in the laptev sea coastal polynya. *J. Geophys. Res.,* **115,** C05015, doi:10.1029/2009JC005798.

Eicken, H., and M. A. Lange, 1989: Development and properties of sea ice in the coastal regime of the southeastern Weddell Sea. *J. Geophys. Res.,* **94,** 8193–8206, doi:10.1029/JC094iC06p08193.

——, M. Lensu, M. Leppranta, W. B. Tucker, A. J. Gow, and O. Salmela, 1995: Thickness, structure, and properties of level summer multiyear ice in the Eurasian sector of the Arctic Ocean. *J. Geophys. Res.,* **100,** 22 697–22 710, doi:10.1029/95JC02188.

Ferry, N., and Coauthors, 2015: Product user manual GLOBAL-REANALYSIS-PHYS-001-004. Marine Environment Monitoring Service, 52 pp. [Available online at http://marine.copernicus.eu/documents/PUM/CMEMS-GLO-PUM-001-004-009-010-011-017.pdf.]

Flocco, D., D. Schroeder, D. L. Feltham, and E. C. Hunke, 2012: Impact of melt ponds on arctic sea ice simulations from 1990 to 2007. *J. Geophys. Res.,* **117,** C09032, doi:10.1029/2012JC008195.

Gow, A. J., S. F. Ackley, W. F. Weeks, and J. W. Govoni, 1982: Physical and structural characteristics of Antarctic sea ice. *Ann. Glaciol.,* **3,** 113–117.

Hibler, W., III, 2001: Sea ice fracturing on the large scale. *Eng. Fract. Mech.,* **68,** 2013–2043, doi:10.1016/S0013-7944(01)00035-2.

Holland, P. R., and D. L. Feltham, 2005: Frazil dynamics and precipitation in a water column with depth-dependent supercooling. *J. Fluid Mech.,* **530,** 101–124, doi:10.1017/S002211200400285X.

Holloway, G., and A. Proshutinsky, 2007: Role of tides in arctic ocean/ice climate. *J. Geophys. Res.,* **112,** C04S06, doi:10.1029/2006JC003643.

Hopkins, M. A., and H. H. Shen, 2001: Simulation of pancake-ice dynamics in a wave field. *Ann. Glaciol.,* **33,** 355–360, doi:10.3189/172756401781818527.

Hunke, E. C., and W. H. Lipscomb, 2010: CICE: The Los Alamos sea ice model documentation and software user's manual, version 4.1. Tech. Rep. LA-CC-06-012, Los Alamos National Laboratory, Los Alamos, NM, 76 pp.

——, D. Notz, A. K. Turner, and M. Vancoppenolle, 2011: The multiphase physics of sea ice: A review for model developers. *Cryosphere,* **5,** 989–1009, doi:10.5194/tc-5-989-2011.

Jacka, T. H., S. F. Allison, R. Thwaiters, and J. Wilson, 1987: Characteristics of the seasonal sea ice of east Antarctica and comparison with satellite observations. *Ann. Glaciol.,* **9,** 85–91.

Jakobson, E., T. Vihma, T. Palo, L. Jakobson, H. Keernik, and J. Jaagus, 2012: Validation of atmospheric reanalyses over the central Arctic Ocean. *Geophys. Res. Lett.,* **39,** L10802, doi:10.1029/2012GL051591.

Jeffries, M. O., and W. F. Weeks, 1992: Structural characteristics and development of sea ice in the western Ross Sea. *Antarct. Sci.,* **5** (1), 63–75.

Jenkins, A., and A. Bombosch, 1995: Modeling the effects of frazil ice crystals on the dynamics and thermodynamics of ice shelf water plumes. *J. Geophys. Res.,* **100,** 6967–6981, doi:10.1029/94JC03227.

Kalnay, E., and Coauthors, 1996: The NCEP/NCAR 40-Year Re-analysis Project. *Bull. Amer. Meteor. Soc.,* **77,** 437–471, doi:10.1175/1520-0477(1996)077<0437:TNYRP>2.0.CO;2.

Kantha, L. H., 1995: A numerical model of arctic leads. *J. Geophys. Res.,* **100,** 4653–4672, doi:10.1029/94JC02348.

Kozo, T. L., 1983: Initial model results for arctic mixed layer circulation under a refreezing lead. *J. Geophys. Res.,* **88,** 2926–2934, doi:10.1029/JC088iC05p02926.

Lange, M. A., 1988: Basic properties of Antarctic sea ice as revealed by textural analysis of ice cores. *Ann. Glaciol.,* **10,** 95–101.

——, S. F. Ackley, and P. Wadhams, 1989: Development of sea ice in the Weddell Sea. *Ann. Glaciol.,* **12,** 92–96.

Levine, M. D., C. A. Paulson, J. Simpkins, and S. R. Gard, 1993: Observations from LEADEX, Beaufort Sea, Arctic Ocean, March–April 1992. COAS Data Rep. 153, Oregon State University, Corvallis, OR, 159 pp.

Markus, T., 1999: Results from an ECMWF-SSM/I forced mixed layer model of the southern ocean. *J. Geophys. Res.,* **104,** 15 603–15 620, doi:10.1029/1999JC900080.

——, and D. Cavalieri, 2000: An enhancement of the NASA team sea ice algorithm. *IEEE Trans. Geosci. Remote Sens.,* **38,** 1387–1398, doi:10.1109/36.843033.

Martin, S., and P. Kauffman, 1981: A field and laboratory study of wave damping by grease ice. *J. Glaciol.,* **27,** 283–313.

Maslowski, W., J. Clement Kinney, M. Higgins, and A. Roberts, 2012: The future of arctic sea ice. *Annu. Rev. Earth Planet. Sci.,* **40,** 625–654, doi:10.1146/annurev-earth-042711-105345.

McDougall, T. J., P. M. Barker, R. Feistel, and B. K. Galton-Fenzi, 2014: Melting of ice and sea ice into seawater and frazil ice formation. *J. Phys. Oceanogr.,* **44,** 1751–1775, doi:10.1175/JPO-D-13-0253.1.

McGuinness, M. J., M. J. M. Williams, P. J. Langhorne, C. Purdie, and J. Crook, 2009: Frazil deposition under growing sea ice. *J. Geophys. Res.,* **114,** C07014, doi:10.1029/2007JC004414.

Morison, J. H., M. G. McPhee, T. B. Curtin, and C. A. Paulson, 1992: The oceanography of winter leads. *J. Geophys. Res.,* **97,** 11 199–11 218, doi:10.1029/92JC00684.

Nakawo, M., and N. Sinha, 1984: A note on brine layer spacing of first-year sea ice. *Atmos.–Ocean,* **22,** 193–206, doi:10.1080/07055900.1984.9649193.

Omstedt, A., 1985: Modelling frazil ice and grease ice formation in the upper layers of the ocean. *Cold Reg. Sci. Technol.,* **11,** 87–98, doi:10.1016/0165-232X(85)90009-6.

——, and U. Svensson, 1984: Modeling supercooling and ice formation in a turbulent Ekman layer. *J. Geophys. Res.,* **89,** 735–744, doi:10.1029/JC089iC01p00735.

Ono, N., 1967: Specific heat and heat of fusion of sea ice. *Physics of Snow and Ice: International Conference on Low Temperature Science 1966 Proceedings,* Vol. 1, H. Oura, Ed., Institute of Low Temperature Science, 599–610.

Petty, A. A., P. R. Holland, and D. L. Feltham, 2014: Sea ice and the ocean mixed layer over the Antarctic shelf seas. *Cryosphere,* **8,** 761–783, doi:10.5194/tc-8-761-2014.

Schwarzacher, W., 1959: Pack-ice studies in the Arctic Ocean. *J. Geophys. Res.,* **64,** 2357–2367, doi:10.1029/JZ064i012p02357.

Schweiger, A., R. Lindsay, J. Zhang, M. Steele, H. Stern, and R. Kwok, 2011: Uncertainty in modeled arctic sea ice volume. *J. Geophys. Res.,* **116,** C00D06, doi:10.1029/2011JC007084.

Skyllingstad, E. D., and D. W. Denbo, 2001: Turbulence beneath sea ice and leads: A coupled sea ice/large-eddy simulation study. *J. Geophys. Res.,* **106,** 2477–2497, doi:10.1029/1999JC000091.

Smedsrud, L. H., 2011: Grease-ice thickness parameterization. *Ann. Glaciol.,* **52,** 77–82, doi:10.3189/172756411795931840.

——, and R. Skogseth, 2006: Field measurements of arctic grease ice properties and processes. *Cold Reg. Sci. Technol.,* **44,** 171–183, doi:10.1016/j.coldregions.2005.11.002.

Steiner, N., 2001: Introduction of variable drag efficients into sea-ice models. *Ann. Glaciol.,* **33,** 181–186, doi:10.3189/172756401781818149.

Svensson, U., and A. Omstedt, 1998: Numerical simulations of frazil ice dynamics in the upper layers of the ocean. *Cold Reg. Sci. Technol.,* **28,** 29–44, doi:10.1016/S0165-232X(98)00011-1.

Tison, J. L., and J. Haren, 1989: Isotopic, chemical and crystallographic characteristics of first-year sea ice from Bried Bay (Princess Ragnhild Coast—Antarctica). *Antarct. Sci.,* **1,** 261–268, doi:10.1017/S0954102089000386.

Vancoppenolle, M., T. Fichefet, H. Goosse, S. Bouillon, G. Madec, and M. A. M. Maqueda, 2009: Simulating the mass balance and salinity of arctic and Antarctic sea ice. 1. Model description and validation. *Ocean Modell.,* **27,** 33–53, doi:10.1016/j.ocemod.2008.10.005.

——, and Coauthors, 2011: Assessment of radiation forcing data sets for large-scale sea ice models in the southern ocean. *Deep-Sea Res. II,* **58,** 1237–1249, doi:10.1016/j.dsr2.2010.10.039.

Wang, S. M., and J. C. Doering, 2005: Numerical simulation of supercooling process and frazil ice evolution. *J. Hydraul. Eng.,* **131,** 889–897, doi:10.1061/(ASCE)0733-9429(2005)131:10(889).

Yu, L., Z. Zhang, M. Zhou, S. Zhong, D. Lenschow, H. Hsu, H. Wu, and B. Sun, 2010: Validation of ECMWF and NCEP–NCAR reanalysis data in Antarctica. *Adv. Atmos. Sci.,* **27,** 1151–1168, doi:10.1007/s00376-010-9140-1.

Zib, B. J., X. Dong, B. Xi, and A. Kennedy, 2012: Evaluation and intercomparison of cloud fraction and radiative fluxes in recent reanalyses over the Arctic using BSRN surface observations. *J. Climate,* **25,** 2291–2305, doi:10.1175/JCLI-D-11-00147.1.